Journal of Geophysical Research: Solid Earth

RESEARCH ARTICLE
10.1029/2018JB015673

Deformation Behavior of Sandstones From the Seismogenic Groningen Gas Field: Role of Inelastic Versus Elastic Mechanisms

R. P. J. Pijnenburg[1], B. A. Verberne[1], S. J. T. Hangx[1], and C. J. Spiers[1]

[1]HPT Laboratory, Department of Earth Sciences, Utrecht University, Utrecht, The Netherlands

Key Points:
- Triaxial tests on reservoir sandstone simulating gas depletion show inelastic strains (30–55% of total)
- Inelastic strain is porosity and rate dependent and develops from the onset of deformation, implying an expanding, porosity- and rate-sensitive yield envelope
- This behavior should be incorporated in geomechanical modeling of reservoir depletion and induced seismicity

Supporting Information:
- Supporting Information S1

Correspondence to:
R. P. J. Pijnenburg,
r.p.j.pijnenburg@uu.nl

Citation:
Pijnenburg, R. P. J., Verberne, B. A., Hangx, S. J. T., & Spiers, C. J. (2018). Deformation behavior of sandstones from the seismogenic Groningen gas field: Role of inelastic versus elastic mechanisms. *Journal of Geophysical Research: Solid Earth*, *123*, 5532–5558. https://doi.org/10.1029/2018JB015673

Received 20 FEB 2018
Accepted 19 JUN 2018
Accepted article online 26 JUN 2018
Published online 17 JUL 2018

Abstract Reduction of pore fluid pressure in sandstone oil, gas, or geothermal reservoirs causes elastic and possibly inelastic compaction of the reservoir, which may lead to surface subsidence and induced seismicity. While elastic compaction is well described using poroelasticity, inelastic and especially time-dependent compactions are poorly constrained, and the underlying microphysical mechanisms are insufficiently understood. To help bridge this gap, we performed conventional triaxial compression experiments on samples recovered from the Slochteren sandstone reservoir in the seismogenic Groningen gas field in the Netherlands. Successive stages of active loading and stress relaxation were employed to study the partitioning between elastic versus time-independent and time-dependent inelastic deformations upon simulated pore pressure depletion. The results showed that inelastic strain developed from the onset of compression in all samples tested, revealing a nonlinear strain hardening trend to total axial strains of 0.4 to 1.3%, of which 0.1 to 0.8% were inelastic. Inelastic strains increased with increasing initial porosity (12–25%) and decreasing strain rate (10^{-5} s^{-1} to 10^{-9} s^{-1}). Our results imply a porosity and rate-dependent yield envelope that expands with increasing inelastic strain from the onset of compression. Microstructural evidence indicates that inelastic compaction was controlled by a combination of intergranular cracking, intergranular slip, and intragranular/transgranular cracking with intragranular/transgranular cracking increasing in importance with increasing porosity. The results imply that during pore pressure reduction in the Groningen field, the assumption of a poroelastic reservoir response leads to underestimation of the change in the effective horizontal stress and overestimation of the energy available for seismicity.

1. Introduction

Fluid extraction from subsurface sandstone reservoirs, in the context of oil, gas, and geothermal energy production, frequently results in surface subsidence (Fialko & Simons, 2000; Morton et al., 2001; Pratt & Johnson, 1926; Sharp & Hill, 1995; van Wees et al., 2014) and sometimes in induced seismicity (Davies et al., 2013; Grasso, 1992; Segall & Fitzgerald, 1998; Suckale, 2009; van Eijs et al., 2006). Both effects are caused by the stress changes due to depletion of pore fluid pressure and the associated reservoir compaction. Depletion-induced subsidence is observed globally in both onshore (Bardainne et al., 2008; Davies et al., 2013; Fialko & Simons, 2000) and offshore settings (Cuisiat et al., 2010; Davies et al., 2013; Santarelli et al., 1998) and may cause damage to buildings and infrastructure (Koster & van Ommeren, 2015; Mitchell & Green, 2017; van der Voort & Vanclay, 2015). The magnitude of subsidence is typically several centimeters to several tens of centimeters. Examples include the Port Neches, Clam Lake, and Caplen oil fields in Texas (4–63 cm; Morton et al., 2001), the giant Groningen gas field in the Netherlands (NAM, 2016), and the Geysers geothermal field, California (40–80 cm; Mossop & Segall, 1997). In fields showing tens of centimeters of subsidence, induced seismicity is often widespread, as seen in the Groningen field, (van Eijs et al., 2006), the Geysers geothermal field in California (Eberhart-Phillips & Oppenheimer, 1984), and the War-Wink gas field in Texas (Doser et al., 1991). Despite these adverse effects, continued exploitation is likely to remain a necessity if we are to meet energy demand, at least in the coming few decades (Brouwer et al., 2016; GEA, 2012; IEA, 2016).

Compaction of reservoir formations and associated surface subsidence and seismicity are driven by the increase in effective stress that accompanies fluid extraction (Zoback, 2007). In sandstones, compaction is for a large part poroelastic (Wang, 2000; Zoback, 2007). However, the systematically observed discrepancy between dynamic (elastic) stiffness moduli derived from well logs, and the 1.2 to 3 times lower static (elastic + inelastic) moduli obtained from triaxial testing, suggests that deformation of reservoir sandstones is in part inelastic (Yale & Swami, 2017). Moreover, some sandstone reservoirs show delayed subsidence after

production initiation (Hettema et al., 2002; van Thienen-Visser et al., 2015), or ongoing subsidence after production has been reduced (Mallman & Zoback, 2007). This too implies that inelastic, time-dependent deformation processes may play a role. Elastic compaction is relatively easily modeled using poroelasticity theory (Altmann et al., 2010; Dzung et al., 2009; Geertsma, 1973). However, inelastic and especially time-dependent inelastic compaction are not, as the underlying deformation mechanisms are still poorly understood and the associated stress versus strain and strain rate behavior is quantified to only a limited extent (Bernabe et al., 1994; Brantut et al., 2013; Brzesowsky, Hangx, et al., 2014; De Waal, 1986; Heap et al., 2015; Shalev et al., 2014).

In sandstone reservoirs in the upper crust (<5 km), inelastic deformation processes include (1) intergranular (grain boundary) microcracking, (2) intergranular slip (Bernabe et al., 1994; Menéndez et al., 1996; Shalev et al., 2014), (3) intragranular and transgranular microcracking (Baud et al., 2000; Wong & Baud, 2012), and (4) intergranular pressure solution (Rutter, 1983; Spiers et al., 2004). While pressure solution is known to be an important deformation mechanism over timescales relevant for sandstone diagenesis (>10,000 years; Tada & Siever, 1989; Yang, 2000), existing rate data (Chester et al., 2004; Dewers & Hajash, 1995; Gratier & Guiguet, 1986; Niemeijer et al., 2002; Renard et al., 1999; Schutjens, 1991; van Noort et al., 2008) suggest that any contribution of this slow creep process to the compaction of quartz-rich reservoir rock will be small over timescales (decades) and temperatures ($T < 150$ °C) relevant for upper crustal fluid extraction. Rather, for these conditions, inelastic deformation in sandstone is expected to be accommodated by the above grain-scale, brittle processes (Baud et al., 2000; Brantut et al., 2013; Guéguen & Fortin, 2013; Heap et al., 2009, 2015; Hol et al., 2018; Menéndez et al., 1996; Tengattini et al., 2014; Wong & Baud, 1999, 2012).

The onset of inelastic deformation by these processes is typically described using a discrete yield criterion, or yield envelope, assumed to be rate insensitive (Baud et al., 2000, 2004, 2006; Klein et al., 2001; Rutter & Glover, 2012; Skurtveit et al., 2013; Tembe et al., 2008; Wong et al., 1997; Wong & Baud, 2012; Zhang et al., 1990). Brittle yield is usually determined at the onset of nonlinear stress-strain behavior, which is associated with shear-coupled dilatancy at low mean effective stresses and with compaction at high mean effective stresses (Wong et al., 1997; Wong & Baud, 2012). This type of brittle deformation behavior in sandstones is well known to be favored by higher initial porosity (Wong & Baud, 2012), since higher porosity leads to higher stress concentrations at grain contacts (Cook et al., 2015; De Freitas & Dobereiner, 1986).

A range of microphysical models has been formulated to explain the above empirical observations (Kemeny & Cook, 1991; Paterson & Wong, 2005; Wong & Baud, 2012). At low mean effective stresses, models for inelastic sand or sandstone deformation invoke (1) intergranular (tensile) grain boundary cracking plus subsequent frictional slip along the boundaries of assumed spherical grains (Guéguen & Fortin, 2013) or (2) intergranular or intragranular (wing-) cracking plus subsequent frictional slip along the newly formed cracked surfaces (Ashby & Sammis, 1990; Baud et al., 2014). In both cases, crack propagation is described by (Griffith-) equilibrium crack growth. At high mean effective stresses, intragranular and transgranular cracking is proposed to be the dominant deformation mechanism, with Mode 1 equilibrium crack extension initiating from flaws at the periphery of assumed Hertzian contacts (Guéguen & Fortin, 2013; Wong et al., 1997; Zhang et al., 1990).

However, such models have limitations. First, grain-to-grain contacts in sandstones are often indented and/or cemented (McBride, 1989) and are hence non-Hertzian. This significantly increases the resistance to grain-scale cracking (Bernabe et al., 1992; Sackfield & Hills, 1986; Wong & Wu, 1995). Second, heterogeneity in the strength of the constituent grains or grain contacts is often neglected. In loose quartz sand, the strength of grains has been shown to be distributed (Brzesowsky et al., 2011), with the weak grains failing in the early stages of deformation (Brzesowsky, Spiers, et al., 2014; Karner et al., 2003). Moreover, inelastic deformation developing at the earliest stages of compression has also been demonstrated for cohesive sandstones (Hol et al., 2018; Shalev et al., 2014). This suggests that at least for these materials, inelastic strain development plus work hardening must occur continuously during loading and that deformation cannot be adequately described by a discrete yield criterion based on the onset of nonlinear stress-strain behavior (Karner et al., 2005, 2003). Third, the effects of time-dependent deformation processes, such as subcritical crack growth, or rate-dependent grain boundary friction have been largely neglected, leaving the rate dependence of the stress-strain and yield behavior of sands and sandstones quantified to only a limited extent (Brantut et al., 2014, 2013; Brzesowsky, Hangx, et al., 2014; De Waal, 1986; Heap et al., 2009, 2015; Karner et al., 2005). Indeed, in many treatments of pressure depletion during oil, gas, or geothermal energy production from sandstone reservoirs, inelastic deformation is neglected completely and reservoir compaction is, in

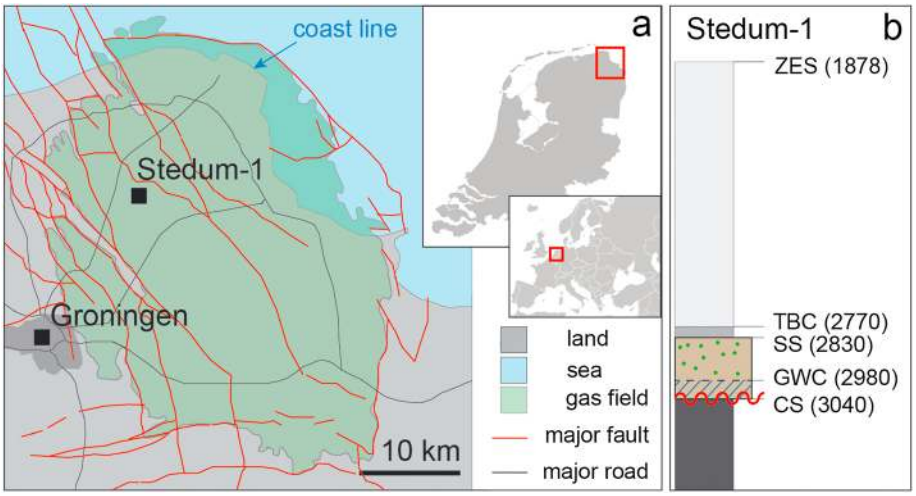

Figure 1. (a) Location of the Groningen gas field in the NE Netherlands and of the Stedum (SDM)-1 well. Major normal faults (i.e., vertical throw >150 m) cutting the Slochteren reservoir at 2,830-m true vertical depth (TVD) are indicated in red. Image modified after NAM (2016). (b) Stratigraphy of the Groningen gas field at the SDM-1 well (http://www.nlog.nl/keuzelijst-boringen). Depths (TVD, in m) to the top of the intersected units are indicated. The gas is present in the upper part of the reservoir (i.e., from 2,830 to 2,980-m TVD in the SDM-1 well). ZES: Zechstein evaporite sequence; TBC: Ten Boer claystone, SS: Slochteren sandstone; GWC: gas-water contact; CS: Carboniferous shale.

first approximation, assumed to be characterized by a simple, elastic compaction coefficient (Altmann et al., 2010; Geertsma, 1973; Lele et al., 2016; Mulders, 2003; van Eijs et al., 2006; Wassing et al., 2016; Zoback, 2007).

However, the evolution of the yield envelope with strain and the effects of loading rate on stress-strain and yield behavior are of key importance in determining the reservoir response to the partitioning between elastic and inelastic strain. This partitioning directly controls the evolution of compaction and hence surface subsidence during production (Mallman & Zoback, 2007; Schutjens et al., 1995), and the stresses (Buijze et al., 2017) and elastic energy available to drive induced seismicity and associated energy dissipating processes occurring upon fault rupture (Cooke & Madden, 2014; Mcgarr, 1999; Shipton et al., 2013). In recent years, the onset of significant induced seismicity in strongly depleted reservoirs, such as the large Groningen field in the NE Netherlands (Grotsch et al., 2011), has created an urgent need to understand these effects much better (e.g., de Waal et al., 2017; Spiers et al., 2017).

This paper addresses this need. We studied the deformation behavior of samples recovered from the reservoir formation at the heart of the vast Groningen gas field, that is, the Slochteren sandstone (Figure 1). To investigate the relative contributions of elastic and inelastic deformation, we performed conventional triaxial compression tests, employing successive stages of axial compression and stress relaxation. The experiments were conducted at applied differential stresses up to 50 MPa, in a manner designed to simulate the effective stress changes accompanying pore pressure depletion in a poroelastic reservoir. A poroelastic stress path was chosen in order to test whether Slochteren sandstones showed purely elastic (reversible) stress-strain behavior under these conditions. Conversely, if inelastic strain would develop, then inelastic deformation should accordingly be expected to occur during field depletion. We used samples with a range of porosities (φ = 12–25%) representing those present in the reservoir. Microstructural analysis of undeformed and deformed samples was used to gain insight into the operating inelastic deformation mechanisms and any influence on these of factors such as porosity, grain size, and grain size distribution. Our results are directly relevant to understanding elastic versus inelastic strain and strain energy partitioning in the Slochteren reservoir sandstone and to understanding the mechanisms controlling depletion-induced reservoir compaction, subsidence, stress evolution, and induced seismicity in the Groningen field and in similar gas fields worldwide.

2. Geological Setting of The Groningen Gas Field and Slochteren Reservoir

The Groningen gas field is an ~30 by 30-km field located in the NE Netherlands (Figure 1a) on the southern flank of the east-west striking southern Permian basin (Glennie, 1972; Ziegler, 1990). Thick continental

sediments were deposited in this basin in the Permian under semiarid to arid conditions, on top of an eroded, upper Carboniferous shale basement (Glennie, 1972; see Figure 1b for the stratigraphy). The Slochteren reservoir sandstone member, now located at about 3 km depth, is approximately 200-m thick and constitutes a generally upward fining succession of conglomerates and fluvial sandstones, overlain by cross-bedded eolian sandstones, muddy siltstones, and ultimately lacustrine mudstones, forming the Ten Boer claystone formation (Waldmann & Gaupp, 2016). A thick sequence (500–1,000 m) of Zechstein evaporites, characterized by a basal anhydrite/dolomite unit (~40 m) and multiple halite units overlies the Slochteren sandstone (Amthor & Okkerman, 1998). Between the Triassic and the Late Jurassic, regional thermal subsidence resulted in burial and NW-SE trending extensional fracturing of the Permian sediments, and hydrocarbons were expelled from the underlying organic-rich Carboniferous shale and coal intervals into the reservoir (de Jager et al., 1996). At present, the Slochteren reservoir consists of a gas-bearing interval and a water-saturated interval, which typically comprise the upper 50–150 m and lower 50–150 m, respectively (NAM, 2013). Since production from the field began in 1963, the pore fluid pressure has decreased from 35 MPa to a surprisingly uniform ~8 MPa (NAM, 2016).

The porosity of the Slochteren sandstone is well constrained from wireline logs and fluid-immersion tests on core plugs, with average values ranging from 18 to 22% in the center of the reservoir, decreasing laterally to 12–16% at the margins (NAM, 2016). The sandstone can be classified as a subarkose to lithic subarkose (McBride, 1963), consisting on average of 72–90 vol% quartz, 8–25 vol% feldspar, 0.5–5.5 vol% clay, and 3–10 vol% of lithic rock fragments, which include basaltic and sedimentary lithoclasts (Waldmann et al., 2014; Waldmann & Gaupp, 2016). During burial diagenesis, the total initial feldspar content was reduced by dissolution reactions, leading to precipitation of kaolinite and illite in the pores and onto the pore walls (Waldmann & Gaupp, 2016).

3. Sample Material and Pore Fluid Chemistry

Samples used in this study were obtained from core material composed of Slochteren sandstone (2,830–3,040-m true vertical depth [TVD]), taken during drilling of the Stedum (SDM)-1 well (Figure 1a) and provided courtesy of the field operator (Nederlandse Aardolie Maatschappij). The SDM-1 well was drilled in 1965, prior to major gas production.

Sets of two to three cylindrical plugs, each 25 mm in diameter and 50–55 mm in length were drilled from the SDM-1 core, at specific depth intervals, in an orientation parallel to the core axis and subperpendicular to the often slightly inclined bedding (within 10°). The ends of the plugs were ground flat and perpendicular to the sample axis using a polishing wheel, to ensure homogeneous load distribution during testing. The resulting samples were homogeneous to slightly laminated. Samples from above and below the gas-water contact were, respectively, gray and red in color. All samples tested in the present study are listed in Table 1. In naming them, the annotations *g* and *w* indicate that the sample was obtained from core taken from the gas-bearing (*g*) or water-saturated (*w*) intervals of the SDM-1 well. Samples with the same number (e.g., Sw07) imply that they were taken from the same depth interval, while suffixes *a* to *c* are used to identify deformed samples. The absence of any suffix indicates that the sample was not deformed in a laboratory test. These undeformed samples were used as benchmark samples to identify deformation-induced microstructural changes.

During core storage, the high-salinity brine present in the core upon recovery resulted in salt precipitation in the pore space. Prior to each experiment, these precipitates were redissolved by vacuum saturating the sample with demineralized water (DMW) to fill it with realistic pore fluid. We determined the corresponding initial porosity (φ_0) using the injected DMW volume, that is, the mass difference between the dry sample (sample + salt precipitates) and the wet sample (sample + salts + DMW), divided by the density of DMW (0.997 g/mL), while taking into account the volume change of the injected fluid upon salt dissolution (see supporting information S1; Waldmann, 2011). The porosity values obtained ranged from 12.7 to 24.6%. The ion concentrations of the resultant pore fluids were determined using inductively coupled mass spectrometry (ICP-MS) and are listed in Table 2 (for analytical details, see S2), where they are compared with previous measurements on in situ pore fluids extracted from the Slochteren sandstone interval of the Zeerijp-3a core, which was retrieved in 2015 at a location 5 km from the SDM-1 well (see Hol et al., 2018).

Table 1
List of Experiments, Conditions, and Key Data

Sample	TVD (m)	φ_0 (%)	$(\sigma_1-\sigma_3)_{max}$ (MPa)	$(e_t)_{fin}$ (%)	$(e_{el})_{fin}$ (%)	$(e_i)_{fin}$ (%)	$(\Delta\varphi_t)_{fin}$ (%)	$(\Delta\varphi_{el})_{fin}$ (%)	$(\Delta\varphi_i)_{fin}$ (%)	$(\sigma_1-\sigma_3)_{max}$ (MPa)	E_a (GPa)	$(e_t)_{fin}$ (%)	$(e_{el})_{fin}$ (%)	$(e_i)_{fin}$ (%)	$(e_i^{inst})_{max}$ (%)	$(e_{cr})_{max}$ (%)	$(e_i^{\Sigma})_{max}$ (%)	$(e_{el}^{\Sigma})_{max}$ (%)	$(\Delta\varphi_t)_{fin}$ (%)	$(\Delta\varphi_{el})_{fin}$ (%)	$(\Delta\varphi_i)_{fin}$ (%)	H/S
In-situ conditioning phase (constant P_c^{eff} = 8 MPa)										*Multi-step phase* (constant P_c^{eff} = 15 MPa)												
Sw09b	3036.6	12.7	23.2	0.35	0.25	0.10	−0.29	−0.19	−0.10	50.4	18.4	0.42	0.31	0.11	0	0.10	0.10	0.32	−0.18	−0.17	−0.01	H
Sw11b	3036.8	14.2	22.4	0.43	0.27	0.16	−0.26	−0.16	−0.10	50.0	20.2	0.38	0.31	0.07	0	0.06	0.06	0.32	−0.22	−0.22	−0.00	H
Sw13a	3044.8	17.4	24.0	0.53	0.27	0.26	−0.32	−0.17	−0.15	50.2	17.7	0.55	0.39	0.16	0	0.16	0.16	0.40	−0.42	−0.26	−0.16	H
Sg09b	2894.1	17.7	24.4	0.50	0.37	0.13	−0.17	−0.05	−0.12	49.0	15.4	0.51	0.34	0.17	0	0.16	0.16	0.35	−0.31	−0.14	−0.17	S
Sg10a	2919.0	18.0	21.7	0.73	0.26	0.47	−0.51	−0.13	−0.38	49.6	13.2	0.77	0.44	0.33	0	0.33	0.33	0.43	−0.43	−0.18	−0.25	H
Sw02a	3053.8	19.9	24.2	0.54	0.30	0.24	−0.30	−0.11	−0.19	49.6	19.1	0.46	0.32	0.14	0	0.15	0.15	0.30	−0.31	−0.18	−0.13	H
Sg05a[a]	2892.6	21.6	-	-	-	-	-	-	-	45.5	9.3	1.16	0.56	0.60	0.06	0.59	0.64	0.51	-	-	-	H
Sg05c	2892.6	21.6	22.1	0.72	0.31	0.41	−0.51	−0.20	−0.31	48.6	9.4	1.30	0.57	0.73	0.16	0.59	0.75	0.53	−0.61	−0.07	−0.54	H
Sw07a	3034.5	24.6	23.8	0.98	0.21	0.77	−0.39	−0.13	−0.26	40.2	7.6	1.27	0.47	0.81	0.12	0.69	0.81	0.49	−0.65	−0.09	−0.56	H

Note. Experiments were performed wet (demineralized water + former brine precipitates; see Table 2), at T = 100 °C and P_p = 10 MPa.
[a]Experiment that was not conditioned to the pre-depleted in situ stress and in which no pore volume data were obtained.
Symbols: TVD: the true vertical depth along the SDM-1core from where samples were derived; φ_0 denotes the initial porosity; $(\sigma_1-\sigma_3)_{max}$ denotes the maximum differential stress imposed on the sample; $(e_t)_{fin}$ and $(\Delta\varphi_t)_{fin}$ denote the total axial strain and total porosity change, respectively, at the end of each phase;$(e_i)_{fin}$ and $(\Delta\varphi_i)_{fin}$ denote the final inelastic axial strain and porosity change, respectively, at the end of each phase;$(e_{el})_{fin}$ and $(\Delta\varphi_{el})_{fin}$ denote the final elastic axial strain and porosity change at the end of each phase, determined using:$(e_{el})_{fin} = (e_t)_{fin} - (e_i)_{fin}$, and$(\Delta\varphi_{el})_{fin} = (\Delta\varphi_t)_{fin} - (\Delta\varphi_i)_{fin}$ respectively; E_a denotes the apparent Young's modulus, inferred from a linear fit of the linear part of the stress-strain curve; $(e_i^{inst})_{max}$ and $(e_{cr})_{max}$ denote the sum of all instantaneous and creep inelastic axial strains accumulated during all the active loading and relaxation stages, respectively, of the multistep phase (see section 6.2.1); $(e_i^{\Sigma})_{max}$ denotes the maximum cumulative inelastic axial strain and is given $(e_i^{\Sigma})_{max} = (e_i^{inst})_{max} + (e_{cr})_{max}$. $(e_{el}^{\Sigma})_{max}$ denotes the maximum cumulative elastic axial strain, calculated using $(e_{el}^{\Sigma})_{max} = (e_t)_{max} - (e_i^{\Sigma})_{max}$. Note that $(e_i^{\Sigma})_{max} \approx (e_i)_{fin}$, and:$(e_{el}^{\Sigma})_{max} \approx (e_{el})_{fin}$; H/S denotes the use of the Heard vessel (H) or the Shuttle vessel (S).

4. Experimental Methods

In this study, we performed combined incremental axial loading plus stress relaxation experiments. These were conducted under conventional triaxial test conditions, with $\sigma_1 > \sigma_2 = \sigma_3 = P_c$ (fixed confining pressure). The experiments consisted of constant strain rate deformation steps ($\dot{\varepsilon} \approx 10^{-5}$ s^{-1}), applied to load the samples to successively higher differential stresses, with each step being followed by a period of stress relaxation at near-constant load-point position (Rutter & Mainprice, 1978). The aim was to investigate the effect of initial porosity on stress-strain and stress versus strain rate behavior, with specific attention for the contribution of elastic versus inelastic strain. All experiments were conducted at a temperature of 100 °C, representative of the top of the Slochteren reservoir in the SDM-1 well (at 2,830-m TVD; see NAM, 2013). We imposed effective stress changes simulating full depletion of the Groningen gas reservoir (i.e., a pore pressure drop from 35 to 0.1 MPa), assuming poroelastic behavior.

4.1. Experimental Apparatus

The experiments were conducted using two conventional triaxial testing machines at the High Pressure and Temperature laboratory at Utrecht University, referred to here as the Heard vessel (described by Hangx et al., 2010b, and Peach, 1991) and the Shuttle vessel (described by Verberne et al., 2013). For a brief description of these essentially equivalent machines, the reader is referred to S3.

4.2. Choice of Applied Stress Path

The stress path applied in the incremental loading steps preceding each stress relaxation interval was chosen to simulate the effective stress changes that we estimate would occur in situ during full depletion of a poroelastically deforming Slochteren reservoir sandstone. Henceforth, we assume that the maximum in situ stress is vertical (following NAM, 2016) and we refer to the vertical stress and to the maximum and minimum horizontal stresses within the reservoir as the maximum (σ_1), intermediate (σ_2), and minimum principal compressive stress (σ_3), respectively.

Prior to gas extraction, σ_1 at the top of the reservoir was 65 MPa (Schutjens et al., 1995), σ_3 was determined to be 43 MPa (Breckels & van Eekelen, 1982), while the pore pressure (P_p) measured 35 MPa (NAM, 2016; Schutjens et al., 1995). This implies a maximum principal effective stress $\sigma_1^{eff} = \sigma_1 - P_p$ of 30 MPa, a minimum principal effective stress $\sigma_3^{eff} = \sigma_3 - P_p$ of 8 MPa, and a differential stress ($\sigma_1 - \sigma_3$) of 22 MPa. The predepletion stress state for the present experiments was chosen to match. We assumed that the vertical overburden stress (σ_1) could be considered constant. Full depletion of the field to a pore pressure of 0.1 MPa then implies an increase in σ_1^{eff} from 30 to ~65 MPa. The concomitant change in σ_3^{eff} can be roughly estimated assuming poroelastic deformation under uniaxial strain conditions (Wang, 2000; Zoback, 2007), using

$$\Delta\sigma_3^{eff} = \alpha\Delta P_p\left(\frac{(1-2\nu)}{(1-\nu)} - 1\right) \quad (1)$$

Assuming a Poisson's ratio (ν) of 0.15 ± 0.05 (as estimated for the Slochteren sandstone by Hettema et al., 2000) and a Biot coefficient (α)

Table 2
Ion Concentration and Density Data for the Pore Fluids Used During Testing of Samples From the Gas-Bearing and Water-Saturated Intervals of the SDM-1 Well

	Ion concentration (mol/L)						Density (g/mL)
	Ca^{2+}	Mg^{2+}	K^{+}	Na^{+}	Cl^{-}	S^{2-}	
Experimental pore fluid:gas interval samples	0.0	0.0	0.1	2.1	1.8	0.1	1.12
Experimental pore fluid:water interval samples	0.1	0.0	0.1	4.0	3.6	0.3	1.23
Reservoir pore fluid (water interval ZRP-3a)	1.0	0.1	0.1	3.4	4.9	0.0	1.21

Note. For comparison, data are shown as obtained for the water-saturated interval of the Slochteren sandstone from the Zeerijp (ZRP-)3a well, drilled in 2015, 5 km from the SDM-1 well (see Hol et al., 2018).

of 1, σ_3^{eff} is thus estimated to increase during depletion from 8 MPa to ~15 ± 2 MPa, resulting in an increase in the differential stress from 22 to ~50 MPa. These changes in $(\sigma_1 - \sigma_3)$ and σ_3^{eff} provided the basis for our choice of loading paths.

We tested our samples in two phases. In the first (in situ conditioning) phase, we imposed the in situ stress conditions expected in the Slochteren sandstone reservoir prior to depletion, that is, $(\sigma_1 - \sigma_3)$ = 22 MPa, at an effective confining pressure ($P_c^{eff} = P_c - P_p$) of 8 MPa. In the second (multistep) phase, stress conditions were imposed that are expected after depletion in an assumed poroelastic reservoir, that is, $(\sigma_1 - \sigma_3)$ up to 50 MPa, and P_c^{eff} = 15 MPa. Poroelastic stress changes were chosen in order to test whether Slochteren sandstone behaved poroelastically under these conditions. Alternatively, if inelastic strains would develop, then inelastic deformation would be expected in the reservoir. If this is the case, the chosen values of $(\sigma_1 - \sigma_3)$ and σ_3^{eff} would represent upper and lower bounds, respectively.

4.3. Experimental Procedure

4.3.1. Testing Procedure

After sample assembly (see S4), our samples were emplaced in the oil-filled triaxial vessel and brought to the testing temperature (T = 100 °C) and pressure conditions (P_c = 18 MPa and P_p = 10 MPa) used during the in situ conditioning phase. This was achieved by increasing the confining and pore pressures in steps, such that the effective confining pressure never exceeded the value used during testing. Subsequently, the loading piston was advanced at a near-constant (within 1% of the determined value) total axial strain-rate ($\dot{\varepsilon}_t$) of 10^{-5} s^{-1}, until a differential stress of 22 MPa was attained. The piston was then arrested, allowing stress relaxation for 24 to 48 hr, until the differential stress $(\sigma_1 - \sigma_3)$ reached a near-constant value, that is, until the decrease in the differential stress fell within the noise on the internal axial load sensor (~0.1 MPa). Following this stress relaxation stage, the sample was tested for reversible loading/unloading behavior, by imposing multiple axial loading/unloading stress cycles of ±2 MPa. The sample was then fully unloaded (i.e., $[\sigma_1 - \sigma_3]$ was returned to 0 MPa), and the effective confining pressure was increased to 15 MPa.

In the subsequent multistep phase, we imposed P_c = 25 MPa and P_p = 10 MPa, so that P_c^{eff} = 15 MPa, at T = 100 °C. We then applied multiple, sequential steps of piston advancement, at $\dot{\varepsilon}_t \approx 10^{-5}$ s^{-1}, to obtain differential stresses of 22, 30, 35, 40, 45, and ultimately 50 MPa (where supportable by the sample). Each loading step was terminated by piston arrest, followed by stress relaxation for 24 hr. Upon completion of the final stress relaxation stage, the sample was unloaded axially, and the confining pressure and pore pressure were removed, maintaining the effective pressure below the test value. After cooling to ~80 °C, the sample assembly was removed from the testing machine, and the sample was extracted for microstructural analysis.

4.4. Data Acquisition and Processing

In processing and presenting our data, we adopt the convention that compressive stresses, compressive axial strains, and dilation are positive. Throughout each experiment, the internal axial load, sample temperature, confining pressure, pore pressure, pore fluid volume change, and axial displacement signals were logged at a frequency of 10 Hz during piston advancement intervals, or else at 0.2 Hz, during intervals of stress relaxation. After application of appropriate corrections, these data were processed (see S5) to yield the total axial strain $\varepsilon_t \approx e_t$ = change in sample length/the initial sample length (for the present low strains), the total porosity change $\Delta\varphi_t$, the differential stress $(\sigma_1 - \sigma_3)$ and the apparent Young's modulus (E_a).

The quantities $(e_t)_{fin}$ and $(\Delta\varphi_t)_{fin}$, tabulated in Table 1, refer respectively to the final total axial strain and the corresponding total porosity change determined at the end of either the in situ conditioning phase, or the multistep phase, assuming zero strain and porosity change at the start of each phase. Thus, in determining $(e_t)_{fin}$ and $(\Delta\varphi_t)_{fin}$ at the end of the multistep phase, we neglected any permanent strains accumulated during the preceding in situ conditioning phase. Since the inelastic strains developed during the in situ conditioning phase were small, this approach resulted in negligible errors in the values determined (<0.4% of the determined value). Similarly, to determine the final inelastic axial strain $(e_i)_{fin}$ and the final inelastic porosity change $(\Delta\varphi_i)_{fin}$ accumulated after either the in situ conditioning phase, or the multistep phase, we divided the permanent change in sample length and pore volume, determined upon axial unloading after finalizing each phase, by the initial sample length L_0 and volume V_0, respectively. Again, in determining $(e_i)_{fin}$ and $(\Delta\varphi_i)_{fin}$ in the multistep phase, any permanent strains accumulated during the preceding in situ conditioning phase were neglected. The final elastic axial strain $(e_{el})_{fin}$ and elastic porosity change $(\Delta\varphi_{el})_{fin}$ were obtained by subtraction of $(e_i)_{fin}$ and $(\Delta\varphi_i)_{fin}$ from $(e_t)_{fin}$, and $(\Delta\varphi_t)_{fin}$, respectively.

Stress relaxation data were used to yield the axial creep strain (e_{cr}), and the axial creep strain rate ($\dot{\varepsilon}_{cr}$) at any instant during relaxation, following the methodology outlined by Rutter and Mainprice (1978; S5). In the present work, the term creep refers to time-dependent deformation at any instant in time and at any magnitude of stress, notably during relaxation stages of the experiments. The relaxation data are used to gain insight into the magnitude of strain rate and any the relationship to imposed stress, as a function of initial porosity.We anticipate that the strain rates measured, at the given stresses and strains,will be comparable at least in order of magnitude terms, to those measured in constant-stress creep tests at similar stresses and strains (e.g., Brantut et al., 2014; Heap et al., 2009, 2015).

4.5. Microstructural Analyses

Microstructural investigation was performed on undeformed SDM-1 core materials and on deformed SDM-1 plugs recovered after experimentation. The undeformed SDM-1 samples consisted of core material left over after drilling cylindrical plugs for mechanical testing. Thus, each plug tested has an undeformed microstructural counterpart (no *a-c* suffix in name), sampled within 2 cm, which we used as a benchmark for assessing experimentally induced microstructural changes. Sectioned samples were imaged in full using scanning electron microscopes, employing backscattered electron (BSE) imaging (see S6; Preibisch et al., 2009; Sakic et al., 2011).

Quantitative microstructural analysis was performed on portions (~10 to 50 mm^2 in size) of stitched images. In the case of undeformed samples, grains were manually delineated using ImageJ software to create grain maps. These maps were used to quantitatively investigate textural features, such as grain size, grain size distribution, grain aspect ratio, and shape-preferred orientation (S6). To estimate the mean crack density in our undeformed and deformed samples, defined here as the total number of cracks normalized to the number of grains analyzed, we employed the linear intercept method (Underwood, 1970). To do this, a square grid of spacing 0.5 mm, measuring 16 mm^2, was superposed onto the BSE photomosaics at a similar location in each sample. Each intersection of a vertical or horizontal gridline with an intragranular or transgranular crack and with a grain was tallied, resulting in crack density measured parallel ($CD_{||}$) and normal ($CD_{\perp}$) to the coring direction or principal compressive stress axis. Crack density data were obtained for all samples except sample Sg05c.

5. Results

5.1. Mechanical Data

A list of the experiments performed, the corresponding test conditions, and key mechanical data is given in Table 1. A list of the key symbols used in this study is given in the appendix.

5.1.1. Mechanical Behavior During the In Situ Conditioning Phase

To illustrate the mechanical behavior of our samples during the in situ conditioning phase, plots of differential stress and total porosity change versus total axial strain data, and differential stress versus time data, are presented in Figure 2, for representative samples of low- (Sw11b; φ_0 = 14.2%) and high-porosity (Sg05c φ_0 = 21.6%) material. All experiments showed concave-up stress-strain behavior up to a differential stress of about 10 MPa, after which near-linear stress-strain behavior was observed (Figure 2a). During the entire

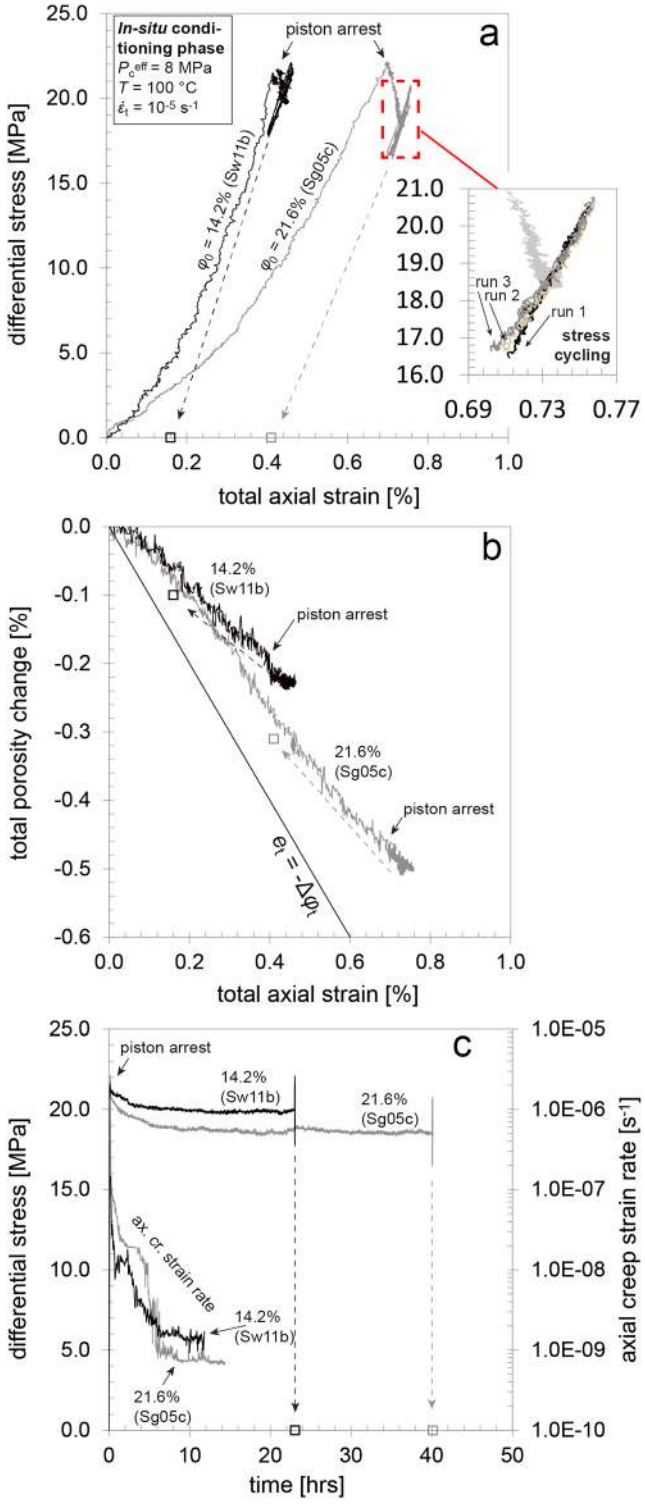

Figure 2. Data obtained during the in situ conditioning phase of the present incremental axial loading plus stress relaxation experiments. Representative plots are shown for low and high porosity samples (φ_0 = 14.2%, Sw11b; φ_0 = 21.6%, Sg05c). (a) Plot showing differential stress versus total axial strain data. During active loading, high porosity samples show more total axial strain than low porosity samples. Inset: after >24 hr of relaxation, stress cycling through ±2 MPa demonstrates reproducible, recoverable (i.e., elastic) deformation. (b) Plot showing total porosity change versus total axial strain data. More compaction (−ve) is observed with increasing initial porosity. (c) Differential stress versus time data. Upon piston arrest, the differential stress relaxes, and the axial creep strain rate decreases from 10^{-6} s^{-1} to $<10^{-9}$ s^{-1}. More relaxation is observed with increasing initial porosity. Open square symbols indicate the final inelastic axial strain $(e_i)_{fin}$ and final porosity change $(\Delta\varphi_i)_{fin}$, obtained after axial unloading of the sample (Table 1).

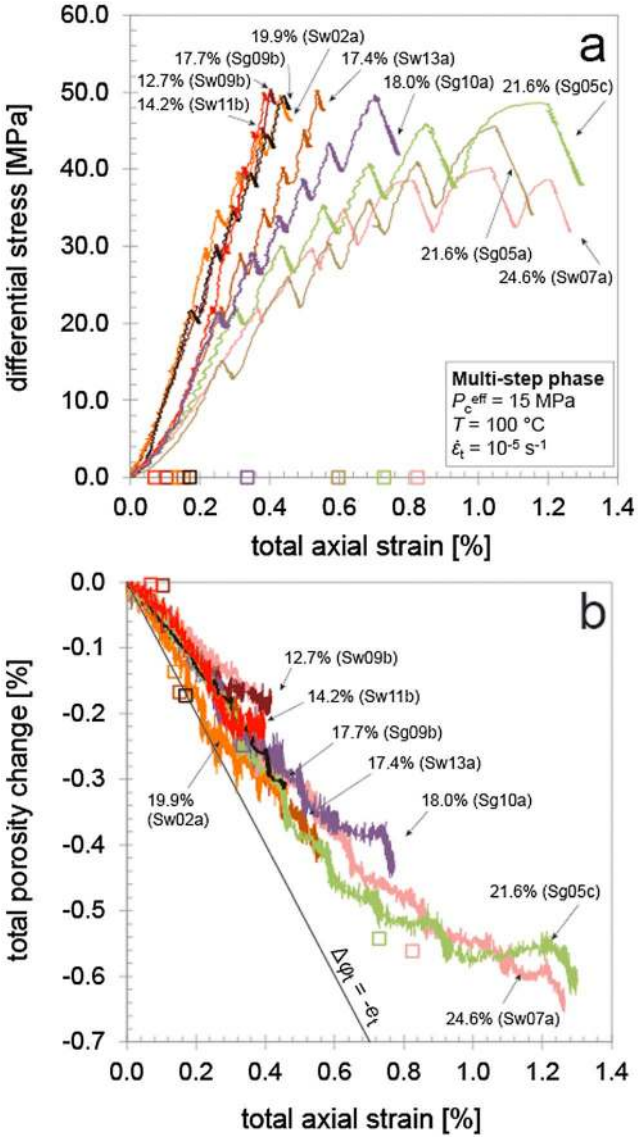

Figure 3. (a) Differential stress and (b) total porosity change ($\Delta\varphi_t$) versus total axial strain (e_t) data obtained from the multistep phase of the incremental axial loading, plus stress relaxation experiments. Initial porosity (φ_0) values are indicated. Samples with high initial porosity show more total axial strain (see a) and compaction ($\Delta\varphi_t < 0$; see b) than samples with low initial porosity. Open square symbols indicate the final inelastic axial strain $(e_i)_{fin}$ and final inelastic porosity change $(\Delta\varphi_i)_{fin}$, determined after unloading (Table 1). For Sg05a, the total porosity change was not determined.

in situ conditioning phase and at all differential stresses, high-porosity samples showed more total axial strain (Figure 2a) and total porosity change (Figure 2b) than low-porosity samples. Within the first 16 hr after piston arrest in the in situ conditioning phase, our data show that the differential stress gradually relaxed by 1 to 4 MPa, after which a near-constant value is reached (Figure 2c). Typically, more stress relaxation and thus higher creep strains were observed with increasing porosity. The axial creep strain rate simultaneously decreased gradually from ~10^{-5} s^{-1} to ~10^{-9} s^{-1}, beyond which the decrease in the differential stress fell within the noise on the internal axial load sensor. After stress relaxation, stress-cycling data show that deformation was nominally reversible, that is, at this point, very little or no additional inelastic axial strain was accumulated during consecutive cycles (Figure 2a, inset). Upon full axial unloading, low-porosity samples ($\varphi_0 < 17.4\%$) typically showed final inelastic axial strains $(e_i)_{fin}$ of 0.1 to 0.2% and final inelastic porosity changes $(\Delta\varphi_i)_{fin}$ of approximately −0.1% (see Table 1). Intermediate porosity samples ($17.4\% \leq \varphi_0 < 21.6\%$) yielded $(e_i)_{fin}$ of 0.1%–0.5% and $(\Delta\varphi_i)_{fin}$ of −0.1 to −0.4%. High-porosity samples ($\varphi_0 \geq 21.6\%$) showed $(e_i)_{fin}$ of 0.4–0.8% and $(\Delta\varphi_i)_{fin}$ of −0.2 to −0.3%.

5.1.2. Mechanical Behavior During the Multistep Phase

In this phase, it will be recalled that samples were subjected to multiple differential stress increments up to a maximum total value of 50 MPa, at P_c^{eff} = 15 MPa. Each stress step was followed by 24 hr of stress relaxation (Figure 3).

During initial active loading up to $(\sigma_1 - \sigma_3) \approx 10$ MPa, all samples showed nonlinear, concave-up stress-strain behavior (Figure 3a). Low-porosity samples ($\varphi_0 < 17.4\%$) showed relatively stiff, near-linear stress-strain behavior during active loading, up to the maximum differential stress imposed (50 MPa), with the apparent Young's moduli (E_a) ranging from 18.4 to 20.2 GPa. These samples showed compaction throughout active loading (i.e., $\Delta\varphi_t < 0$; Figure 3b). During each relaxation stage, the differential stress decreased by typically 1–2 MPa, while the total axial strain increased slightly (Δe_t = 0.005 to 0.015%) and the total porosity change ($\Delta\varphi_t$) remained approximately constant. After unloading, the final inelastic axial strains ($(e_i)_{fin}$ ~0.1%; Table 1) were slightly greater than the final inelastic porosity changes ($(\Delta\varphi_i)_{fin}$ ~0.0%).

Intermediate porosity samples ($17.4\% \leq \varphi_0 < 21.6\%$) showed similar behavior to the above (Figure 3a) but were generally less stiff, and their behavior was less reproducible, with more total axial strain occurring in Sw13a (φ_0 = 17.4%) and Sg10a (φ_0 = 18.0%), than in Sw02a (φ_0 = 19.9%), and Sg09b (φ_0 = 17.7%). During active loading, most stress-strain curves showed near-linear, to just concave-down behavior at $(\sigma_1 - \sigma_3) > 10$ MPa. Values for E_a ranged from 13.2 to 19.1 GPa. All intermediate porosity samples showed compaction throughout active loading (Figure 3b). However, at values of differential stress close to the maximum differential stress imposed, Sg10a showed less compaction with increasing axial strain than was observed at lower differential stresses. During the relaxation stages, the differential stress decreased by 2–8 MPa. For each relaxation stage, the increase in total axial strain amounted to 0.01–0.07% (Figure 3a), while compaction was observed (−0.01 to −0.06%; Figure 3b). After unloading, $(e_i)_{fin} \approx -(\Delta\varphi_i)_{fin}$, that is, the final inelastic axial strains and porosity changes were in the range of 0.1 to 0.3%, and −0.1 to −0.3%, respectively (see Figure 3b).

High-porosity samples ($\varphi_0 \geq 21.6\%$) showed more total axial strain (Figure 3a) and total porosity change (Figure 3b) than lower porosity samples during individual active loading increments. At

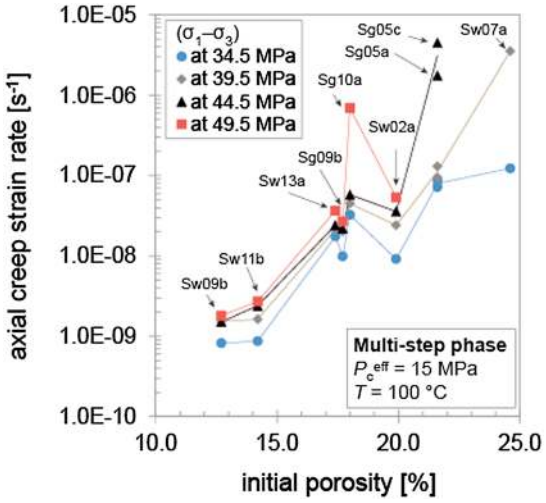

Figure 4. Axial creep strain rate versus initial porosity data obtained during stress relaxation at the differential stresses shown, in the multistep phase of the present experiments. Axial creep strain rates tend to increase with initial porosity and differential stress. Note the increase in sensitivity of creep strain rate to differential stresses at values ≥39.5 MPa and porosities of 18.0% (Sg10a) and those ≥21.6% (Sw07a, Sg05a, and Sg05c). The total axial strains corresponding to each data point are visible in Figure 3a.

$(\sigma_1 - \sigma_3) > 10$ MPa, near-linear, to mildly concave-down stress-strain behavior was seen during active loading, with E_a ranging from 7.6 to 9.4 GPa. Highly concave-down stress-strain behavior was observed beyond differential stresses of 44 MPa (Sg05a), 45 MPa (Sg05c), and 38 MPa (Sw07a). Beyond these stresses, samples showed strain hardening at a decreasing rate, toward a peak strength of 40 to 49 MPa at $e_t \approx 1\%$ (Figure 3a). The target differential stress of 50 MPa could not be achieved. In these samples, the rate of total porosity change with total axial strain (i.e., the slope in Figure 3b) decreased with increasing axial strain, becoming even dilatant at the highest axial strains reached (Sg05c). During the relaxation stages, the differential stress decreased from 2 to 12 MPa. The total axial strain accumulated per relaxation stage ranged from 0.02 to 0.10%, while the total porosity change per stage constituted −0.04 to −0.07%. Upon unloading, $(e_i)_{fin} > -(\Delta\varphi_i)_{fin}$, that is, the final inelastic axial strains were in the range of 0.7 to 0.8%, while the final inelastic porosity changes were approximately −0.5%.

For each sample tested in the multistep phase, the axial creep strain rate ($\dot{\varepsilon}_{cr}$) during stress relaxation was determined at differential stresses of 34.5, 39.5, 44.5, and 49.5 MPa. The results are plotted against initial porosity (φ_0) in Figure 4. Generally, $\dot{\varepsilon}_{cr}$ increased with increasing initial porosity and differential stress. At a constant differential stress of 34.5 MPa, an absolute increase in φ_0 of 5% resulted in an increase of $\dot{\varepsilon}_{cr}$ of about an order of magnitude. At $\varphi_0 \leq 17.7\%$, an increase in $(\sigma_1 - \sigma_3)$ of 5 MPa resulted in an increase of $\dot{\varepsilon}_{cr}$ by only a factor of 1.2–2. However, the sensitivity of $\dot{\varepsilon}_{cr}$ to $(\sigma_1 - \sigma_3)$ increased markedly at higher φ_0 and $(\sigma_1 - \sigma_3)$. Indeed, our sample with $\varphi_0 = 18.0\%$, and all samples with $\varphi_0 \geq 21.6\%$ showed an increase in $\dot{\varepsilon}_{cr}$ of more than an order of magnitude after a 5 MPa stress increase at differential stresses ≥39.5 MPa (Sw07a), 44.5 MPa (Sg05a and Sg05c), or 49.5 MPa (Sg10a). At these differential stresses, the corresponding total axial strains fell in the range of 0.6 to 0.8% (Figure 3a).

5.2. Microstructural Data

5.2.1. Undeformed Samples

Examples of BSE micrographs obtained from undeformed Slochteren sandstone with low ($\varphi_0 = 12.7\%$; Sw09) and high porosity ($\varphi_0 = 24.6\%$; Sw07) and corresponding grain maps are presented in Figure 5. The

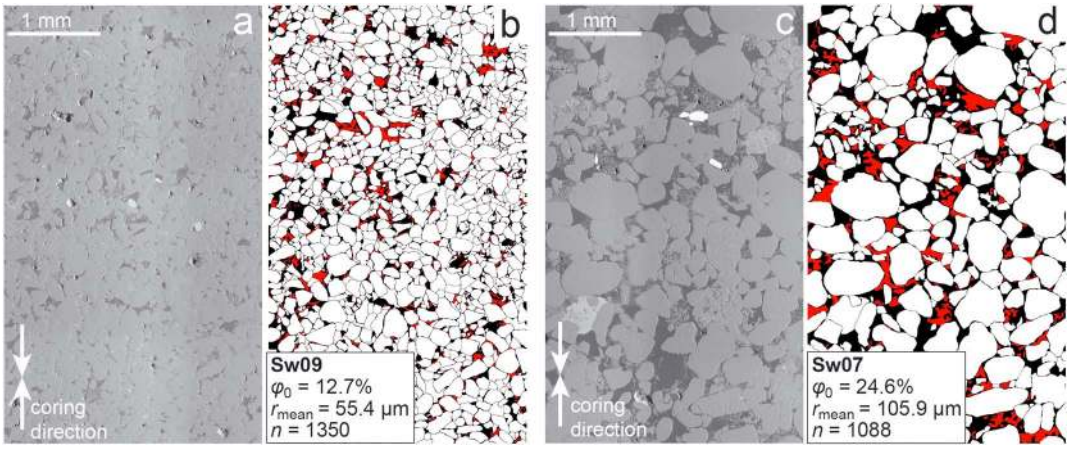

Figure 5. BSE micrographs of undeformed Slochteren sandstone. (a) Micrograph of one of our low-porosity samples ($\varphi_0 = 12.7\%$, Sw09) and (b) the corresponding grain map used for quantitative analysis of textural features (supporting information S7). Grains and porosity are indicated respectively in white and black, while clay minerals are indicated in red. Values of the mean equivalent grain radius (r_{mean}) and the number of grains analyzed (n) are indicated. (c) Micrograph of one of our high porosity samples ($\varphi_0 = 24.6\%$, Sw07) and (d) the corresponding grain map.

Table 3
Intragranular/Transgranular Crack Density (CD) Data of BSE Micrographs of Undeformed and Deformed Samples, Using the Line Intercept Method in a Direction Parallel (||) or Perpendicular (⊥) to the Coring Direction and/or to σ_1

Undeformed				Deformed		
Sample	φ_0	$CD_{\|\|}$	$CD\perp$	Sample	$CD_{\|\|}$	$CD\perp$
	[%]	# per grain	# per grain		# per grain	# per grain
Sw09	12.7	0.08	0.10	Sw09b	0.08	0.11
Sw11	14.2	0.03	0.06	Sw11b	0.03	0.08
Sw13	17.4	0.03	0.05	Sw13a	0.05	0.06
Sg09	17.7	0.09	0.12	Sg09b	0.06	0.11
Sg10	18.0	0.09	0.10	Sg10a	0.17	0.32
Sw02	19.9	0.06	0.07	Sw02a	0.13	0.10
Sg05	21.6	0.14	0.11	Sg05a	0.32	0.63
Sw07	21.6	0.07	0.09	Sw07a	0.28	0.72

Note. In each micrograph, ~ 400 grains were analyzed. Crack density analysis was not performed on sample Sg05c.

quantitative textural data obtained for our samples are described in detail in the supporting information (S7). In general terms, individual samples showed mean equivalent grain radii of quartz and feldspar grains in the range of 30 to 110 μm (S7). These grains were subrounded, and slightly elongated in shape, with a mean aspect ratio of 1.7 (S7). Both quartz and feldspar grains showed indentations at grain-to-grain contacts, suggesting that intergranular pressure solution was active prior to gas production (Figure 5). Data on crack densities (mean number of cracks per grain) measured in the undeformed samples are given in Table 3. Crack densities measured along gridlines parallel to the coring direction ($CD_{||}$) ranged from 0.03 to 0.14 per grain, while those measured along lines perpendicular to the coring direction ($CD\perp$) fell within a similar range of 0.05 to 0.11 per grain. Within these ranges, a clear trend between the crack density and the initial sample porosity was lacking, although the highest values were observed in one of our high-porosity samples Sg05 (φ_0 = 21.6%). The observed similar values of $CD_{||}$ versus $CD\perp$ imply a lack of preferred crack orientation (Table 3).

5.2.2. Deformed Samples

Where observed in our samples, brittle deformation localized near (within ~15 mm) the top and bottom of each sample. Therefore, the present microstructural analysis and crack density determination are performed within regions measuring 5–15 mm from the top of each sample. For these regions, BSE micrographs of microstructures recovered from deformed samples Sw11b, Sw13a, Sg10a, and Sw07a, having porosities of 14.2, 17.4, 18.0, and 24.6%, respectively, are shown in Figure 6. Crack density data obtained for all deformed samples (except Sg05c) are listed in Table 3, where they are compared with the data for the equivalent undeformed material. In all deformed samples studied, intragranular and transgranular cracks (indicated by white arrows in Figure 6) typically emanated from grain-to-grain contacts. In all low-porosity ($\varphi_0 < 17.4\%$) samples (e.g., Sw11b, Figure 6a) and all intermediate-porosity ($17.4\% \leq \varphi_0 < 21.6\%$) samples, except Sg10a (e.g., Sw13a, Figure 6b), mean crack densities were low and similar to those seen in their undeformed counterparts (Table 3). By contrast, intermediate-porosity sample Sg10a (Figure 6c), and all high-porosity samples ($\varphi_0 \geq 21.6\%$; *e.g.* Sw07a; Figure 6d), showed a crack density that was 2 to 8 times higher than obtained in their undeformed counterparts. In these samples, most of the observed cracks were orientated subparallel to the compression direction, that is, $CD\perp > CD_{||}$ (Table 3). In some grains, cracking was pervasive, resulting in triangular crushed zones developing at grain-to-grain contacts (e.g., inset, Figure 6d). None of our deformed samples showed any evidence for the operation of intergranular pressure solution beyond pressure solution features already present in the starting material (Figure 5).

6. Discussion

Incremental axial loading plus stress relaxation experiments on Slochteren sandstone have shown that inelastic deformation played a significant role in all samples, during both the in situ conditioning and the multistep phases, contributing to 0.1–0.8% of inelastic axial strain, versus ~0.3–0.6% of elastic axial strain, in each phase (Table 1). Hence, at the end of each phase, the final inelastic strains were similar in magnitude to the elastic component. During the multistep phase, a substantial part of this inelastic strain represented time-dependent deformation ($(e_{cr})_{fin} \approx$ 0.1–0.7%; Table 1), accumulated during the stress relaxation stages (i.e., 6 days in total). In particular, samples with high initial porosity ($\varphi_0 \geq 21.6\%$) showed pronounced inelastic deformation (Figure 3) and marked acceleration of axial creep strain rates during relaxation at differential stresses above ~41 ± 4 MPa (Figure 4). For the initial porosities and stress conditions explored in this study, the total axial strains (0.4 to 1.3%) and total porosity changes (−0.2 to −0.7%) measured were small and are not expected to result in significant changes in permeability or wave propagation properties. However, given the substantial Groningen reservoir thickness (100–200 m), these small strains may lead to significant reservoir compaction of decimeters and hence potentially to fault reactivation and seismicity (Bourne et al., 2014; Buijze et al., 2017; Spiers et al., 2017). In addition, the partitioning of inelastic versus elastic strain directly influences the energy budget available within the reservoir interval for seismicity (Cooke & Madden, 2014).

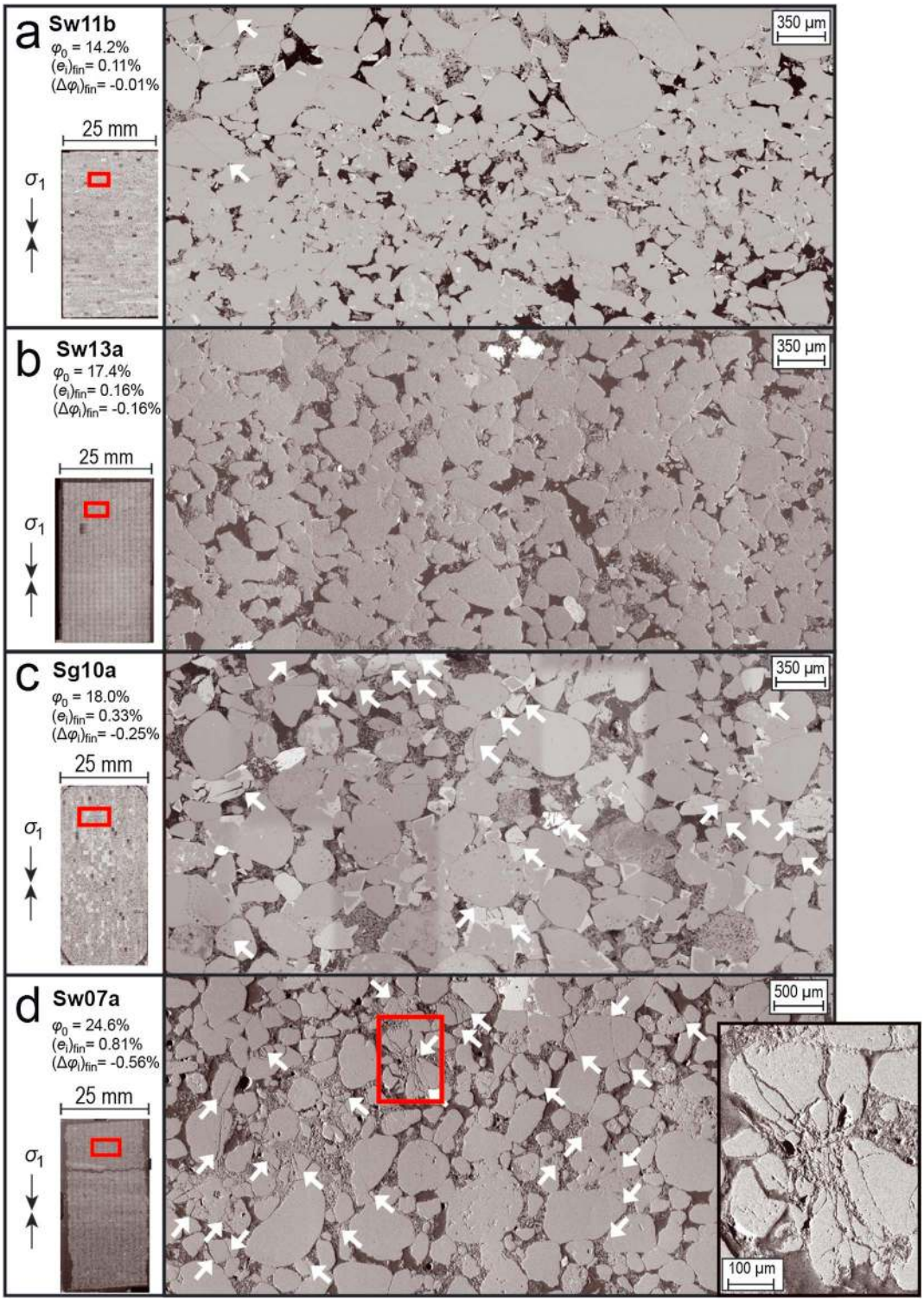

Figure 6. BSE micrographs of postdeformation microstructures. White arrows indicate intra/transgranular cracks. In (a) low-porosity samples (e.g., Sw11b; φ_0 = 14.2%) and (b) intermediate-porosity samples (e.g., Sw13a; φ_0 = 17.4%), these are only sporadically observed, except in the case of (c) intermediate-porosity sample Sg10a (φ_0 = 18.0%), which shows abundant intragranular/transgranular cracks. (d) Micrograph of high-porosity sample Sw07a, showing abundant intragranular/transgranular cracks. The inset depicts two grains showing pervasive crushing at the grain contact. Where observed, intragranular/transgraular cracks emanate from grain-to-grain contacts and tend to be orientated subparallel to the main compressive axis (σ_1). Final inelastic axial strains $(e_i)_{fin}$ and final inelastic porosity changes $(\Delta\varphi_i)_{fin}$ developed during the multistep phase are indicated on the left of the micrographs.

In the following, we will first discuss potential causes for the observed inelastic strain development during the in situ conditioning phase of our experiments. We go on to discuss the magnitudes of inelastic versus elastic deformation, at various differential stresses (cf. depletion) imposed in the multistep phase, and any effect on these of initial porosity and strain rate. The microphysical mechanisms controlling inelastic deformation in the multistep phase and specifically during relaxation stages are discussed, and we evaluate the effects of initial porosity, loading, or strain rate, and progressively increasing strain on yield and yield envelope behavior. Finally, we apply our results to assess the effects of elastic versus inelastic strain partitioning in the Slochteren sandstone reservoir during production of the Groningen field on the evolution in situ stresses, subsidence, and the elastic energy available to drive induced seismicity.

6.1. Inelastic Strain Development During In Situ Conditioning

During the in situ conditioning phase of our experiments (Figure 2), the final inelastic axial strain developed in our samples ranged from 0.1 to 0.8%, versus 0.2 to 0.4% of elastic axial strain, while the final inelastic porosity change ranged from −0.1 to −0.4%, versus −0.1 to −0.2% of elastic porosity change (Table 1). Initial hysteresis in stress-strain behavior is well known in a wide range of materials (e.g., Darling, 2004; Guyer, 2006) and in sandstone is typically attributed to the closure of and semirecoverable displacements along preexisting cracks (David et al., 2012; Walsh, 1965). Such cracks may have been present in situ or have been introduced upon depressurization during coring (Holt et al., 2000), via core drying during storage (Santarelli & Dusseault, 1991), or during sample preparation. Nonetheless, the fully recoverable stress-strain behavior seen during stress cycling (Figure 2a) at stress conditions simulating the predepleted in situ stress state of the Slochteren sandstone suggests that by imposing these conditions in the in situ conditioning phase, any preexisting damage causing inelastic strain was largely removed.

6.2. Inelastic Versus Elastic Deformation During the Multistep Phase

6.2.1. Magnitude: Effects of Porosity and Strain Rate

To fully characterize the stress versus inelastic and elastic strain behavior during the multistep phase, and the effects on these behaviors of initial porosity and strain rate, we must quantify (1) the time-independent (instantaneous) inelastic axial strain developed during active loading (e_i^{inst}), (2) the time-dependent inelastic axial (creep) strain developed during stress relaxation stages (e_{cr}), and (3) the sum of these, that is, the cumulative inelastic axial strain ($e_i^{\Sigma} = \Sigma e_i^{inst} + \Sigma e_{cr}$). In our analysis, e_i^{inst} was calculated by subtracting the linear (i.e., quasi-elastic; see Bernabe et al., 1994) part of the stress-strain curve, characterized by the apparent Young's modulus (E_a), from the total axial strain achieved in each active loading interval, using $e_i^{inst} = e_t - (\sigma_1 - \sigma_3)/E_a$. Values of E_a ranged from 7 to 20 GPa (Table 1) and typically decreased with increasing initial sample porosity (cf. Chang et al., 2006). Inelastic axial creep strain (e_{cr}) developing during relaxation stages was quantified using the methodology outlined by Rutter and Mainprice (1978; see S5). Knowing e_i^{Σ}, the cumulative elastic axial strain (e_{el}^{Σ}) was calculated by subtracting the obtained cumulative inelastic axial strain from the total axial strain. The quantities $(e_i^{inst})_{max}$, $(e_{cr})_{max}$, $(e_i^{\Sigma})_{max}$, and $(e_{el}^{\Sigma})_{max}$, tabulated in Table 1, refer respectively to the maximum instantaneous inelastic axial strain and maximum axial creep strain, and the maximum cumulative inelastic and elastic axial strains, determined by summing up all preceding contributions at the end of the multistep phase of each experiment. This means that $(e_i^{\Sigma})_{max}$ and $(e_{el}^{\Sigma})_{max}$ should be equal to respectively the final inelastic axial strain $(e_i)_{fin}$ and the final elastic axial strain $(e_{el})_{fin}$, which were determined independently from comparison of the piston position before and after the multistep phase (Table 1).

Upon achieving the highest differential stress in any active loading stage, subsequent relaxation of this differential stress was accompanied by progressively developing creep strains, while the creep strain rate decreased (Figures 2a and 2c; see also Rutter & Mainprice, 1978). This implies that the magnitude of inelastic strain achieved after imposing a given differential stress must be strain rate dependent. To investigate this rate dependence, we employ our relaxation data obtained in the multistep phase to approximate the expected stress versus inelastic and elastic strain curves, in the case that our samples were continuously compressed (i.e., in the absence of relaxation stages) at reference strain rates of $\dot{\varepsilon}_t \sim 10^{-5}$ s^{-1}, or at $\dot{\varepsilon}_t \sim 10^{-9}$ s^{-1}, under the present experimental conditions. To that end, we determined e_{el}^{Σ} and e_i^{Σ} at $\dot{\varepsilon}_{cr} \sim 10^{-5}$ s^{-1} and $\dot{\varepsilon}_{cr} \sim 10^{-9}$ s^{-1} and plotted these values versus the differential stress attained at the end of each preceding active loading stage (i.e., at the onset of relaxation) in Figure 7.

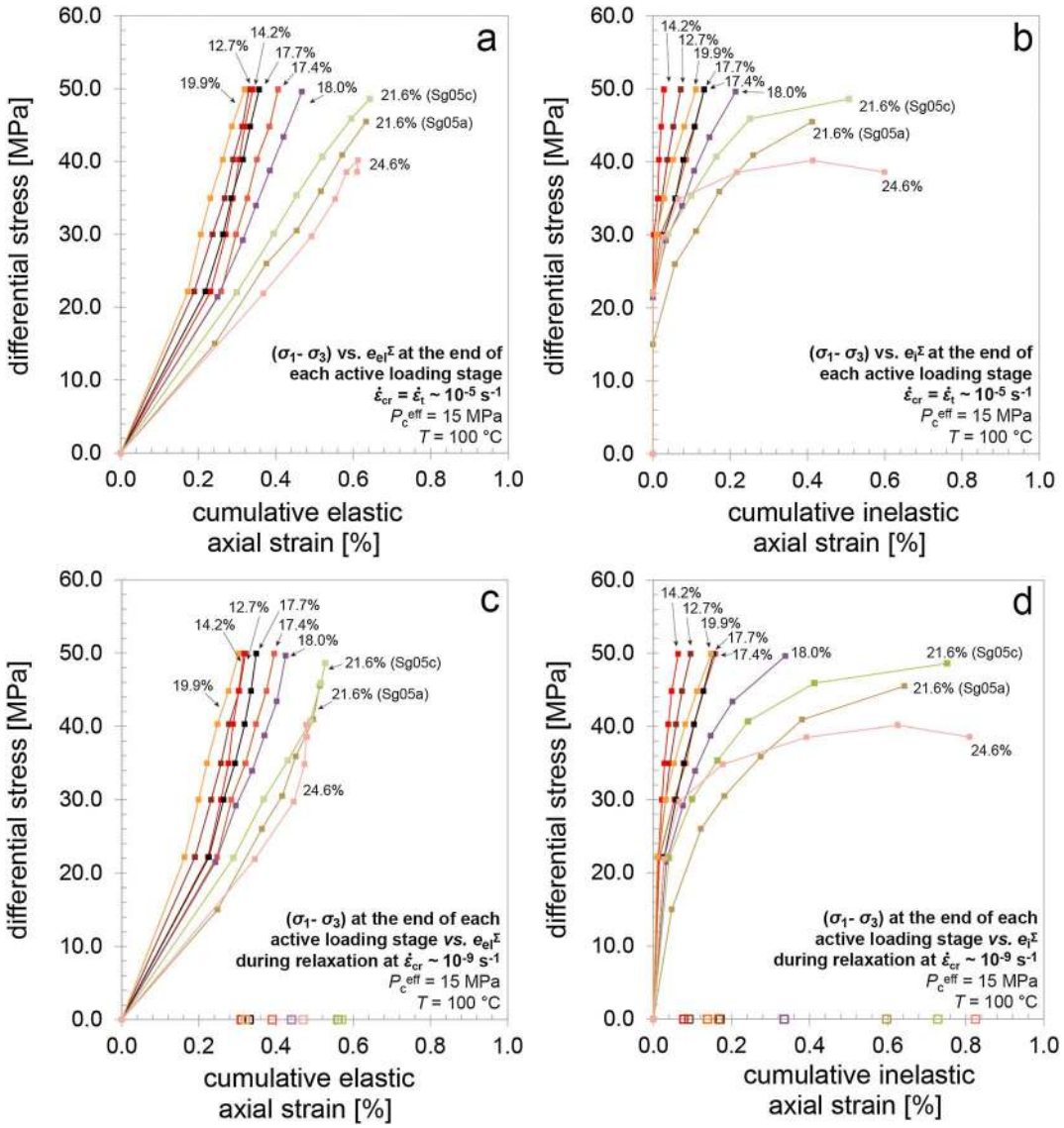

Figure 7. (a) Plot showing differential stress ($\sigma_1 - \sigma_3$) versus cumulative elastic axial strain (e_{el}^{Σ}) data obtained in the multi-step phase at the end of each active loading stage where $\dot{\varepsilon}_{cr} \approx \dot{\varepsilon}_t \approx 10^{-5}$ s^{-1}. Initial porosities (φ_0) of individual curves are indicated. (b) Differential stress versus cumulative inelastic axial strain (e_i^{Σ}) data, obtained at $\dot{\varepsilon}_{cr} \sim 10^{-5}$ s^{-1}. These curves show nonlinear strain-hardening trends, which are more pronounced with increasing φ_0. (c) Curves showing the ($\sigma_1 - \sigma_3$) at the end of each active loading stage versus e_{el}^{Σ} data obtained at $\dot{\varepsilon}_{cr} \sim 10^{-9}$ s^{-1}. At this strain rate, and ($\sigma_1 - \sigma_3$) > 30 MPa, high-porosity samples show less elastic strain than observed at $\dot{\varepsilon}_{cr} \sim 10^{-5}$ s^{-1}. Final elastic axial strains $(e_{el})_{fin}$ are indicated by open square symbols. (d) Curves showing ($\sigma_1 - \sigma_3$) at the end of each active loading stage versus e_i^{Σ} obtained during relaxation stages at $\dot{\varepsilon}_{cr} \sim 10^{-9}$ s^{-1}. At these lower reference strain rates, e_i^{Σ} is measured even in the first relaxation stage at ($\sigma_1 - \sigma_3$) ~22 MPa. Final inelastic axial strains $(e_i)_{fin}$ are indicated by open square symbols.

Before proceeding with our analysis, we note that the resultant ($\sigma_1 - \sigma_3$) versus e_{el}^{Σ} curves determined at $\dot{\varepsilon}_{cr} \sim 10^{-5}$ s^{-1} (Figure 7a) are lower bounds for the expected elastic behavior at the reference strain rate of $\dot{\varepsilon}_t \sim 10^{-5}$ s^{-1} (i.e., least compliant end-members), since creep deformations developing during the preceding relaxation stages have partly dissipated the accumulated elastic strain. For the expected inelastic behavior at these reference strain rates, the ($\sigma_1 - \sigma_3$) versus e_i^{Σ} curves determined at $\dot{\varepsilon}_{cr} \sim 10^{-5}$ s^{-1} (Figure 7b) represent upper bounds (i.e., most compliant end-members), as they include creep strains that have developed during preceding relaxation stages at creep rates lower than 10^{-5} s^{-1}. By contrast, the curves depicted in Figure 7b ($\dot{\varepsilon}_{cr} \sim 10^{-5}$ s^{-1}) are lower bounds for the inelastic behavior expected at the reference strain rate of $\dot{\varepsilon}_t \sim 10^{-9}$ s^{-1}, since e_i^{Σ} increases with decreasing strain rate. An upper bound is given by the differential

stresses and strains obtained at $\dot{\varepsilon}_{cr} \sim 10^{-9}$ s^{-1}. Indeed, more realistic inelastic and elastic behavior in the case of continuous loading at $\dot{\varepsilon}_t \sim 10^{-9}$ s^{-1} is expected to fall in between these upper and lower bounds, such as given by curves describing the $(\sigma_1 - \sigma_3)$ at the end of each active loading stage, versus e_{el}^{Σ} (Figure 7c), and e_i^{Σ} (Figure 7d), determined at $\dot{\varepsilon}_{cr} \sim 10^{-9}$ s^{-1}.

From Figure 7 we observe the following five key points. First, both e_{el}^{Σ} and e_i^{Σ} increased with increasing initial porosity. Second, for both reference strain rates investigated, e_i^{Σ} increased nonlinearly with differential stress (Figures 7b and 7d). Specifically, our samples exhibited continuous inelastic strain hardening, at decreasing hardening rates, except in the highest-porosity sample (φ_0 = 24.6%, Sw07a), which showed minor inelastic strain softening at $e_i^{\Sigma} > 0.6\%$. Third, for the reference strain rate of ~10^{-9} s^{-1}, inelastic strain was measured at all corresponding differential stresses (i.e., $e_i^{\Sigma} > 0$, at all stresses plotted in Figure 7d), even during the first relaxation stage at $(\sigma_1 - \sigma_3)$ ~22 MPa. Fourth, in our low- to intermediate-porosity samples ($\varphi_0 \leq 19.9\%$), both the cumulative inelastic and elastic strains are virtually independent of the reference strain rate (Figure 7). Fifth, in our high-porosity samples ($\varphi_0 \geq 21.6\%$), e_i^{Σ} ranged from 0.4 to 0.6%, measured at $\dot{\varepsilon}_{cr} \sim 10^{-5}$ s^{-1} (Figure 7b), and increased to 0.6 to 0.8%, measured at $\dot{\varepsilon}_{cr} \sim 10^{-9}$ s^{-1} (Figure 7d), while the cumulative elastic strain was 0.6% at $\dot{\varepsilon}_{cr} \sim 10^{-5}$ s^{-1} (Figure 7a) and decreased to 0.4 to 0.5%, at $\dot{\varepsilon}_{cr} \sim 10^{-9}$ s^{-1} (Figure 7c).

The above noted sensitivity of the cumulative elastic and inelastic axial strains to initial porosity is similar to the porosity dependence of elastic and inelastic strains observed in previous triaxial tests on Slochteren sandstone (Hol, Mossop, et al., 2015; Hol et al., 2018; Schutjens et al., 1995) and other types of sandstone (e.g., Wong & Baud, 2012; Wong et al., 1997).Time-, hence, rate-dependent inelastic deformation behavior has been documented previously (Brantut et al., 2013; Heap et al., 2009, 2015), although often at higher differential stresses ($[\sigma_1 - \sigma_3]$ = 50 to 400 MPa) than relevant for upper crustal hydrocarbon (or hydrothermal) fields, such as the Groningen gas field ($[\sigma_1 - \sigma_3] \leq 50$ MPa). In addition, our data show an apparent rate dependence of the stress versus cumulative elastic axial strain curves (Figures 7a and 7c). This is due to the fact that during relaxation, elastic strain stored in the sample and apparatus is partly converted into time-dependent deformation (Rutter & Mainprice, 1978). In the case of our high-porosity samples, at $(\sigma_1 - \sigma_3) > 30$ MPa, substantial stress relaxation of 5–12 MPa was observed in each relaxation stage (Figure 3a), leading to the conversion into permanent strain of most or even all elastic strain accumulated in the foregoing active loading stage (Figure 7d). The implications of the time-dependent deformation behavior observed in our experiments are that conventional stress-strain curves obtained in loading at constant strain or loading rate will depend on the strain or loading rate imposed and that the strain represented will always consist of an elastic and inelastic component.

6.2.2. Effect of Porosity on Inelastic Deformation Mechanisms

As discussed in section 1, inelastic deformation can be caused by intergranular (grain boundary) cracking, intergranular slip, intragranular/transgranular cracking, and intergranular pressure solution (IPS). The microstructures of our deformed samples (Figure 6) showed no evidence that IPS played a role in our experiments. Indeed, assuming a spherical grain radius of 100 μm, φ_0 = 20%, and conditions similar to those imposed in our experiments (σ_1 = 65 MPa, P_p = 35 ➔0.1 MPa, and T = 100 °C), previous work on the kinetics of IPS in quartz (Dewers & Hajash, 1995; Niemeijer et al., 2002; Schutjens, 1991; van Noort et al., 2008) suggests axial creep strain rates by IPS of approximately 10^{-13} s^{-1} at small reductions of P_p, increasing to 10^{-12} s^{-1} at full depletion of the field. By comparing these strain rates with the creep rates $>10^{-10}$ s^{-1} obtained in our experiments (Figure 4), we infer that IPS did not play a role in controlling inelastic strain accommodation in our experiments. However, the rates obtained for IPS fall within 1 order of magnitude from the strain rates derived from the reservoir compaction and surface subsidence data obtained in the Groningen field (10^{-12} s^{-1}; NAM, 2015). Therefore, and given the uncertainties on the existing rate data for IPS (e.g., Spiers et al., 2004), we cannot completely exclude IPS from playing a role in the field.

However, at least for shorter timescales, numerous laboratory studies have shown that low-temperature ($T < 150$ °C) inelastic deformation of sandstone is accommodated by a combination of grain-scale cracking and grain boundary slip (Baud et al., 2000; Brantut et al., 2013; Heap et al., 2009, 2015; Menéndez et al., 1996; Wong & Baud, 1999, 2012). Moreover, previous studies, including stress cycling data (Shalev et al., 2014), microstructural analyses of lab-deformed samples (Bernabe et al., 1994; DiGiovanni et al., 2007; Ord et al., 1991), acoustic emission data (David et al., 2001; Menéndez et al., 1996), and discrete element

modeling (Estrada et al., 2010a, 2010b; Shen et al., 2016) suggest that for a wide range of sandstones, intergranular cracking plus intergranular slip is the dominant deformation mechanism accommodating any inelastic strains in the earlier stages of compression, that is, at low stresses. These intergranular processes may initiate at grain contacts that are particularly weak (uncemented, poorly sutured, or clay-coated) and/or favorably oriented with respect to the principal stresses. When grain contact stresses become sufficiently high, pervasive intragranular or transgranular cracking begins to occur. The present experiments on low and intermediate initial porosity samples ($\varphi_0 < 21.6\%$) showed small inelastic axial strains developing throughout compression (up to 0.1–0.3%; Figure 7d), whereas the corresponding microstructures showed little or no increase in crack density per grain (Table 3). By contrast, in samples with a high initial porosity ($\varphi_0 \geq 21.6\%$), significantly larger inelastic strains of 0.6 to 0.8% were observed at $(\sigma_1 - \sigma_3) > 30$ MPa (Figure 7d), while the micrographs of these samples revealed a marked increase in the density of intragranular/transgranular cracks (Table 3). Furthermore, samples showing increased crack densities yielded $CD_{\perp} > CD_{||}$, implying a preferred orientation of cracks parallel to the main compression direction σ_1. Therefore, it is likely that the increase in e_i and $\Delta\varphi_i$ at $\varphi_0 \geq 21.6\%$ is related to the observed increased role of intragranular/transgranular cracking. Thus, we infer that the mechanisms controlling inelastic strain accommodation in the Slochteren sandstone, under the present experimental conditions, involve mainly intergranular cracking plus intergranular slip at low porosity, with an increasingly important role being played by intragranular/transgranular cracking with increasing initial porosity. However, how intragranular/transgranular cracking contributes to strain is less clear-cut. Intragranular/transgranular cracks may contribute to strain by either (1) pervasive grain contact fragmentation (e.g., Figure 6d, inset), combined with fragment rearrangement (Zhang et al., 1990), or (2) (partial) loss of the load-bearing capacity of a grain, leading to increased loading of the surrounding grains, which in turn may trigger further grain-scale deformation (Brzesowsky, Spiers, et al., 2014), in a larger, potentially localizing volume. Resolving how such processes influence strain and strain localization would require quantitative microstructural investigation of pretest and posttest samples, including microstrain analysis and/or particle tracking. We reserve this for future work.

6.2.3. Effect of Porosity on the Rate Dependence

Predictions of induced compaction and seismicity in sandstone reservoirs, in the context of oil, gas, or geothermal energy exploitation, require constraints on the amount of both time-independent compaction (instantaneous) and time-dependent compaction (Hettema et al., 2002; Mallman & Zoback, 2007; NAM, 2016; van Thienen-Visser et al., 2015). In the present experiments (6 days in total), most of the measured inelastic strain developed during the 24 hr relaxation intervals, so is time dependent (0.1–0.7%; see Table 1), with relatively little inelastic axial strain accumulating instantaneously, in the brief periods of active loading (0.1–0.2%). We note that the importance of time-independent versus time-dependent deformation is defined by the timescale of observation, and time-dependent deformation observed over the present lab timescales (days) may therefore be considered to be time independent over timescales relevant for reservoir production (decades). However, longer-term creep tests performed on Slochteren sandstone have demonstrated ongoing deformation after a period of several months, yielding very low strain rates of $\sim 10^{-11}$ s^{-1} (Hol, van der Linden, et al., 2015, Hol, Mossop, et al., 2015). To quantify the importance of time-dependent deformation over reservoir production timescales, a mechanical model is required that is based on the physical processes driving time-dependent deformation in sandstone. It is therefore important to explore what mechanisms controlled time-dependent deformation in our experiments, in order to assess their influence under both lab and field conditions.

During relaxation intervals in the present experiments, the axial creep strain rate decreased with decreasing differential stress (Figure 2c). The dependence of creep strain rate on differential stress in sandstones is often described using an exponential relation (Brantut et al., 2013, 2014; Heap et al., 2009, 2015; Rijken, 2005), of the form

$$\dot{\varepsilon}_{cr} \propto \exp(B[\sigma_1 - \sigma_3]) \tag{2}$$

where B is an empirical constant whose magnitude is often linked to the process or processes operating during creep (Brantut et al., 2013, 2014; Heap et al., 2009, 2015). For instance, in sandstone experiments where creep has been associated with stress-corrosion cracking, B is typically in the range of 0.1–1.0 (Brantut et al., 2013; Heap et al., 2009, 2015).

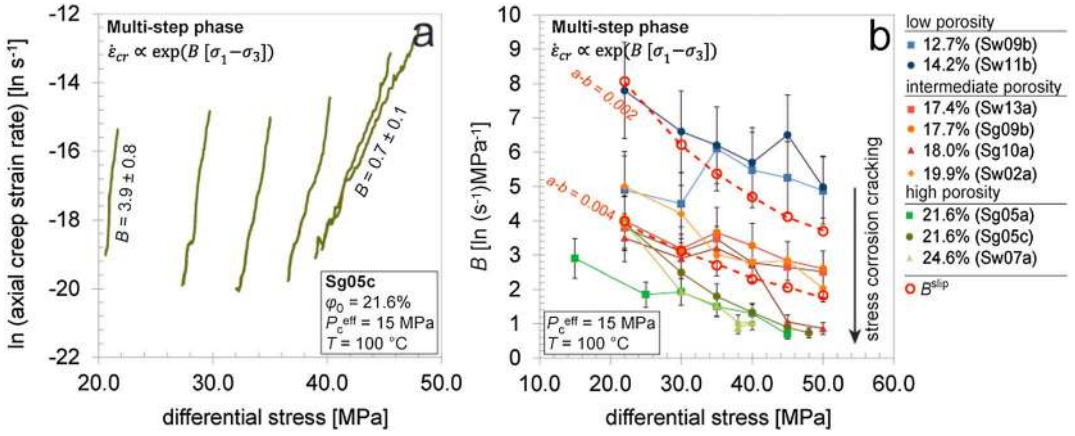

Figure 8. (a) Plot showing the natural logarithm of our axial creep strain rate data versus differential stress, obtained on sample Sg05c (φ_0 = 21.6%) during stress relaxation stages of the multistep phase. To describe the stress sensitivity of the axial creep rates, we assume an exponential relation of the form $\dot{\varepsilon}_{cr} \propto \exp(B\,[\sigma_1 - \sigma_3])$. The stress sensitivity B, determined by linear regression of $\ln(\dot{\varepsilon}_{cr})$ versus $(\sigma_1 - \sigma_3)$ data, decreases with increasing differential stress. (b) Plot showing exponent B versus differential stress data, obtained for each relaxation stage within the multistep phases, of all samples. B decreases with increasing differential stress and porosity. Error bars resultant from linear regression are indicated. The exponent B^{slip}, describing the rate dependency of time-dependent intergranular slip, was determined using previously described rate-and-state friction parameters ($[a - b]$ = 0.002 to 0.004) of unconsolidated Slochteren sandstone gouge material (Hunfeld et al., 2017). Since B^{slip} was similar to B values of our low- and intermediate-porosity samples, we infer that the creep accommodating mechanisms in these samples was predominantly rate-dependent intergranular slip, with an increasing role of stress-corrosion cracking with increasing porosity.

We determined B for each stress relaxation interval of the multistep phase of our incremental axial loading plus stress relaxation experiments, using linear regression of ln $(\dot{\varepsilon}_{cr})$ versus $(\sigma_1 - \sigma_3)$ data, as shown for one of our high-porosity samples (φ_0 = 21.6%; Sg05c) in Figure 8a. The error obtained in B in the linear regression analysis is ± 10–20% of the determined value. For the complete set of experiments, the value obtained for B ranged from 0.7 to 8.4 and, generally, decreased with increasing differential stress and increasing initial porosity (Figure 8b). At the highest differential stresses imposed (40–50 MPa), samples with $\varphi_0 \geq 21.6\%$ and sample Sg10a (φ_0 = 18.0%) showed B values in the range of 0.7–0.9. These values are within the range previously described for creep associated with stress corrosion cracking (Brantut et al., 2013; Heap et al., 2009, 2015). However, at lower differential stress and porosity, B was higher than typically described for stress corrosion cracking, suggesting that for these samples and conditions, a different mechanism controlled time-dependent deformation. Moreover, from their microstructure, most samples with $\varphi_0 < 21.6\%$ (except Sg10a) were inferred to deform predominantly by intergranular cracking and slip, rather than by intragranular/transgranular cracking (Figure 6). Thus, in these samples, mixed intergranular cracking plus frictional slip seems the most likely mechanism controlling creep rates.

This hypothesis will now be analyzed further by examining the expected rate dependency of frictional intergranular slip (see also Karner et al., 2005). Such a rate dependency is widely documented in friction experiments performed on loose, granular gouge materials (*e.g.* Scholz, 2002). It is measured experimentally by imposing direct or rotary shear deformation on a thin layer of gouge material, at constant effective normal stress (σ_n), while measuring the change of the steady state shear stress (τ), and hence of the friction coefficient ($\mu = \tau/\sigma_n$), upon a change in the sliding velocity (v). The resultant rate-dependency of μ is often expressed using the empirical rate-and-state friction (RSF) relation (Marone, 1998):

$$\mu - \mu_0 = a \ln\left(\frac{v}{v_0}\right) + b \ln\left(\frac{v_0 \Omega}{D_c}\right) \tag{3}$$

where μ_0 is a reference friction coefficient, measured at a reference sliding velocity v_0, Ω is a state variable, here taken to be equal to $(d\Omega/dt - 1)(D_c/v)$ (following Dieterich, 1972, 1978), D_c is a characteristic sliding distance over which strength evolution takes place, and a and b are constants, reflecting the

magnitude of the so-called direct and evolution effect on μ occurring after a stepwise change in sliding velocity. For changes in the steady state friction resulting from a stepwise change in sliding velocity, this relation yields

$$a - b = \frac{\mu_{ss} - \mu_0}{\ln \frac{v}{v_0}} \tag{4}$$

(e.g., Marone, 1998). In recent direct-shear experiments performed at our laboratory on gouge material derived from Slochteren sandstone, under similar conditions to those imposed here (T = 100 °C, effective normal stress σ_n = 40 MPa, pore fluid 4.4 M NaCl brine), the steady state friction coefficient μ was found to be 0.61 at v = 1 μm/s, while ($a - b$) ranged from 0.002 to 0.004 (Hunfeld et al., 2017). These values, combined with equation (4), provide a description of the rate dependence of the steady state resistance offered by the Slochteren gouge to simulated fault slip.

This rate dependence of bulk gouge friction can be related to intergranular friction in the gouge experiments and hence to grain boundary friction ($\tilde{\mu}$) in our sandstone experiments, using the microphysical model described by Niemeijer and Spiers (2007) for frictional rate dependence in granular aggregates (N-S model). Assuming that during relaxation intervals strain is achieved by frictional sliding along intergranular interfaces that are already broken during the preceding piston advancement intervals, that is, neglecting any effect of intergranular cohesion, then in the N-S model, μ is related to $\tilde{\mu}$ by

$$\mu = \frac{\sin\Psi + \tilde{\mu}\cos\Psi}{\cos\Psi - \tilde{\mu}\sin\Psi} \tag{5}$$

where Ψ is the dilatancy angle or the average grain contact angle over which slip occurs. Combining this with equation (4) as shown in S8 (Bouckovalas et al., 2003; Xenaki & Athanasopoulos, 2003), the stress dependence of the creep strain rate in the end-member case that creep of our sandstone samples is controlled by intergranular slip is given:

$$\dot{\varepsilon}_{cr}^{slip} \approx \dot{\varepsilon}_{cr,0}^{slip} \exp\left(\frac{1}{a-b}\left(\frac{(\sigma_1-\sigma_3)\sin(2\theta)}{(\sigma_1+\sigma_3)+(\sigma_1-\sigma_3)\cos(2\theta)} - \left(\frac{(\sigma_1-\sigma_3)\sin(2\theta)}{(\sigma_1+\sigma_3)+(\sigma_1-\sigma_3)\cos(2\theta)}\right)_0\right)\right) \tag{6}$$

Here $\dot{\varepsilon}_{cr,0}^{slip}$ denotes the initial axial creep strain rate immediately upon piston arrest and is equal to the axial strain rate imposed during active loading (~10^{-5} s^{-1}). The angle θ is that between σ_1 and the normal to grain boundaries that are optimally orientated for slip and is related to grain boundary friction through $2\theta = \tan^{-1}(-1/\tilde{\mu})$. In turn, $\tilde{\mu}$ is determined from the bulk gouge experiments and applying the N-S model to be 0.28, so that θ is equal to 52.8° (S8). Using this value of θ and values of ($a - b$) of 0.002 and 0.004 (Hunfeld et al., 2017), we employed equation (6) to calculate $\dot{\varepsilon}_{cr}^{slip}$ for the same range of differential stress as imposed in our experiments (0–50 MPa). The stress sensitivities of $\dot{\varepsilon}_{cr}^{slip}$ (B^{slip}) were then determined from linear regression of plots showing $\ln[\dot{\varepsilon}_{cr}^{slip}]$ versus differential stress (cf. equation (2)), at ($\sigma_1 - \sigma_3$) = 22, 30, 35 40, 45, and 50 MPa (Figure 8b).

From Figure 8b it is clear that the dependence of B^{slip} on differential stress obtained is similar to the stress dependence of experimentally obtained B values. For ($a - b$) = 0.002, B^{slip} decreased from 8.0 at low differential stress, to 3.7 at high differential stress, while for ($a - b$) = 0.004, B^{slip} was 4.0 at low differential stress, decreasing toward 1.8 with increasing differential stresses. For each differential stress tested, these values of B^{slip} are roughly similar to the values of B obtained for our low- (φ_0 = 12.7 and 14.2%) and intermediate-porosity samples (φ_0 = 17.4 and 19.9%). For high porosities, B^{slip} was similar to the experimental B values only at the lowest differential stresses tested (22 MPa). At higher differential stresses, B values were lower than values of B^{slip}, where the lowest values of 0.7 to 1.0, measured at ($\sigma_1 - \sigma_3$) = 38 to 50 MPa fell within the range described for creep associated with stress-corrosion cracking (B = 0.1–1.0; Heap et al., 2009, 2015; Brantut et al., 2013). Moreover, these high-porosity samples showed a marked increase in crack density (Table 3). Thus, we infer that creep in our low- and intermediate-porosity samples was predominantly controlled by intergranular slip, while with increasing porosity, the contribution of stress-corrosion cracking within grains increased (i.e., intragranular and transgranular crack growth and ultimate failure). We explain this inference by noting that for the range of stress conditions explored, grain contact stresses developing during

compression of low-porosity samples may not be sufficiently high to activate pervasive (intragranular) stress-corrosion cracking. Rather, in these samples, the relatively small creep strains measured (≤0.3%) are likely accommodated by intergranular slip, occurring at weakly cemented, weakly sutured, or clay-coated grain contacts and/or those favorably oriented with respect to the principal stress axes.

6.3. Expanding Yield Envelope: Effects of Strain and Strain Rate on Inelastic Deformation

Previous studies have characterized the onset of inelastic deformation in sandstone of a given porosity using a discrete yield criterion, assumed to be rate insensitive (Baud et al., 2004, 2006; Menéndez et al., 1996; Skurtveit et al., 2013; Tembe et al., 2007; Wong et al., 1997; Wong & Baud, 2012; Zhang et al., 1990). Typically, the yield point is determined as the point of departure from linear stress-strain behavior, which is associated with the start of dilatancy at low mean effective stresses, and the start of enhanced compaction (in a mean effective stress P versus $\Delta\varphi_t$ plot) at high mean effective stresses (Wong et al., 1997). However, our axial loading plus stress relaxation experiments have demonstrated that inelastic strain develops at all differential stresses imposed, and for all porosities tested (Figure 7d). Such inelastic strains developing from the onset of compression have also been demonstrated during hydrostatic testing of Berea and Darley Dale sandstone (Shalev et al., 2014). Therefore, the above definition of discrete yielding does not adequately describe how inelastic deformation is accommodated in these sandstones. Rather, the continuous accumulation of inelastic strain in our samples, combined with the observed strain hardening (Figures 7b and 7d), implies a yield envelope, which expands continuously with each active loading (at $\dot{\varepsilon}_t \sim 10^{-5}$ s^{-1}) plus stress relaxation step (see also Brzesowsky, Spiers, et al., 2014; Karner et al., 2005, 2003; Shalev et al., 2014; Wong et al., 1992). Furthermore, the magnitude of inelastic strain was shown to increase with decreasing strain rate and increasing initial porosity (Figures 7b and 7d). Hence, the yield envelope for each sample must be one that expands with increasing inelastic strain, increasing loading or strain rate and decreasing initial porosity.

To explain the observed continuous yielding observed throughout our experiments, we note that the bulk strength of a material is determined by its weakest component (Brzesowsky, Spiers, et al., 2014, 2011; Diaz et al., 2003; Lawn, 1993; Lu et al., 2002; Weibull, 1951). In sandstone, the strength-determining components are either the grains or the intergranular grain contacts (Cook et al., 2015; Saidi et al., 2003; Yin & Dvorkin, 1994). The strength of grains increases with grain size (Borg et al., 1960; Brzesowsky, Spiers, et al., 2014; Brzesowsky et al., 2011; Chuhan et al., 2002; Hangx et al., 2010a). Because of this grain size dependency, the lognormal grain size distribution observed in our samples (S7) will inherently result in distributed grain strength. If we assume that the strength of the grain contacts is also distributed, it follows that the weakest grains or grain contacts will fail even in the early, elastically dominated stages of compression, leading to small increments of inelastic strain (Brzesowsky, Spiers, et al., 2014; Karner et al., 2003). As the differential stress increases, larger numbers of grains or grain contacts will fail, resulting in an increasingly larger contribution to inelastic strain. This would lead to a nonlinear increase of inelastic strain with increasing differential stress, such as observed in our experiments (Figures 7b and 7d).

7. Implications

7.1. Effect of Elastic Versus Inelastic Deformation on Reservoir Stress Changes

Reducing the pore pressure in a reservoir from 35 MPa to 0.1 MPa will lead to an increase of the effective horizontal stress (Zoback, 2007). Specifically, in the case of a poroelastic reservoir compacting under the generally assumed uniaxial strain conditions, and assuming $v = 0.15$ and $\alpha = 1$, the effective horizontal stress increases from 8 MPa to ~15 MPa (equation (1)). We assumed such a poroelastic stress evolution in choosing the stress path to be applied in our axial loading experiments. However, this study has shown that compaction of Slochteren sandstone is at none of the conditions tested completely poroelastic (Figure 7d), with final inelastic axial strains ranging from 0.1 to 0.8%, versus 0.3 to 0.6% of elastic axial strain (Table 1). Moreover, some of our experiments showed inelastic radial expansion, that is, $(e_i)_{fin} > -(\Delta\varphi_i)_{fin}$ (Figure 3b). This behavior is especially evident in our samples with $\varphi_0 \geq 21.6$, which show $(e_i)_{fin}$ in the range of 0.7–0.8%, versus $(\Delta\varphi_i)_{fin}$ values of ~ −0.5%.

Under uniaxial strain conditions assumed to be prevalent in the reservoir, the addition of inelastic radial expansion to poroelastic radial expansion will result in an enhanced increase of the effective horizontal stress during depletion. This implies that for our samples with $\varphi_0 \geq 21.6\%$, the experimentally imposed changes in the effective horizontal stress (σ_3^{eff} = 8 to 15 MPa) and differential stress ($[\sigma_1 - \sigma_3]$ = 22 to 50 MPa)

underestimate and overestimate, respectively, the changes in σ_3^{eff} and $(\sigma_1 - \sigma_3)$ upon field depletion. The maximum change in the effective horizontal stress that may occur is found by considering the end-member case in which all axial compression is transferred into radial expansion (zero volume change), so that $\Delta\sigma_3^{eff} = \Delta\sigma_1^{eff} = -\Delta P_p$. Assuming an initial (predepletion) value for σ_3^{eff} of 8 MPa (Breckels & van Eekelen, 1982), this would imply that upon full depletion of the field ($\Delta P_p = -35$ MPa), the effective horizontal stress would increase from 8 to 43 MPa, at a constant differential stress of 22 MPa. In reality, the horizontal stress evolution is likely to fall in between this maximum value and that predicted by assuming a purely poroelastic response (equation (1)). Interestingly, the effective horizontal stresses measured in situ within the Groningen field at the current pore pressure of 8 MPa yield values that are significantly higher ($\sigma_3^{eff} \approx 24$–$31$ MPa) than anticipated assuming poroelastic deformation ($\sigma_3^{eff} \approx 13$ MPa), at least at the few localities determined (van Eijs, 2015). This appears to confirm an inelastic contribution to production-induced reservoir compaction.

The above further implies that for our high-porosity samples ($\varphi_0 \geq 21.6\%$), the poroelastic stress changes imposed, and the strains measured, are unlikely to be representative for the in situ stress evolution and compaction of high-porosity regions within the Groningen field. Instead, stress changes developing in these high-porosity regions are more likely to follow the yield envelope as it expands with increasing strain. Near faults, such stress changes may influence fault rupture and seismicity, which warrants further analysis of the evolution of the expanding yield envelope with strain and concomitant effects on in situ stress development and stress evolution along irregular faults. To date, though, any influence of inelastic deformation of the reservoir rock on stress changes and seismicity has been neglected in fault rupture models developed for the Groningen field (Buijze et al., 2017; Lele et al., 2016; Mulders, 2003; van den Bogert, 2015; van Eijs et al., 2006; Wassing et al., 2016). Future modeling work needs to take these effects into account.

7.2. Implications for Induced Seismicity

In the context of hydrocarbon production from sandstone reservoirs, reactivation of preexisting faults and associated seismicity may occur when (offset) strata along a fault compact by a different amount, that is, in the case of differential compaction (Mulders, 2003; van Eijs et al., 2006). Differential compaction may be accommodated by gradual, inelastic fault slip, thus dissipating the developing strain in a virtually aseismic manner. Alternatively, differential compaction may not initially cause fault slip, resulting in elastic and/or inelastic distortion of the surrounding reservoir rock and an increase of the shear stresses acting on the fault (Jaeger et al., 2007; Scholz, 2002). The elastic component of this deformation leads to energy storage, whereas any inelastic deformation dissipates energy. Once these shear stresses exceed the resistance of the fault to slip, rupture will follow, leading to release of the stored elastic strain energy accumulated within the fault and surrounding reservoir system. This release occurs by various processes such as frictional heating, inelastic asperity deformation, wall-rock damage, pore pressure changes and fluid flow, rupture propagation, and grain size reduction (gouge formation; Cooke & Madden, 2014; Shipton et al., 2013), while only a small proportion (5 to 20%) is consumed in generating seismic waves (Mcgarr, 1999). It follows that discriminating inelastic from elastic reservoir compaction is important for estimating the seismic energy budget. However, as already indicated, most existing seismological models assume a linear poroelastic response of the reservoir to pore pressure depletion (e.g., Lele et al., 2016). The assumption of poroelastic reservoir deformation is also employed in the fault strain versus seismicity model formulated by Bourne et al. (2014, 2015), although these authors did allow for partitioning between seismic from aseismic strain energy developing within faults.

The mechanical response of the reservoir to depletion is often quantified using a simple compaction coefficient or an apparent stiffness (S_a), given $S_a = -\Delta P_p/\Delta e_t$. This apparent stiffness is frequently obtained from mechanical plug testing data (Hettema et al., 2000; Hol, Mossop, et al., 2015; Schutjens et al., 1995), surface subsidence data (Ketelaar, 2009; NAM, 2015), and/or in situ compaction data (NAM, 2015). Note, though, that since Δe_t denotes the change in the total axial strain, the apparent stiffness includes both elastic and inelastic contributions. Values of S_a obtained from mechanical testing of Slochteren sandstone plugs show a relatively wide range, notably from 3 to 30 GPa (Hettema et al., 2000; NAM, 2016). For comparison with surface subsidence data, we apply the most simple approach to estimate S_a from these data, by assuming that $\Delta e_t = \Delta L/L_0$. Here ΔL is the amount of surface subsidence and L_0 is the initial reservoir thickness. Inserting values measured at the SDM-1 well for $\Delta L = 0.35$ m, $L_0 = 200$ m, and $\Delta P_p = -27$ MPa (NAM, 2016), we obtain $S_a = 15$ GPa. In situ compaction measurements, based on the displacement of radioactive markers located along the reservoir intersection of the SDM-1 well, show slightly more compliant S_a values, ranging from 9–13 GPa (NAM, 2015).

To determine the elastic contribution to induced reservoir compaction, and hence the percentage of total strain energy available for seismicity, we now apply our strain-partitioning data (Figure 7) to determine both the apparent stiffness S_a and the elastic stiffness, given $S_{el} = -\Delta P_p/\Delta e_{el}^{\Sigma}$. Since the stress changes imposed on our samples with $\varphi_0 \geq 21.6\%$ may not be representative for stress changes developing in high-porosity regions within the Groningen field (see section 7.1), we exclude these results from the present analysis. Neglecting any influence of the small inelastic radial expansions ($(e_i)_{fin} > -(\Delta\varphi_i)_{fin}$; Figure 3b) measured in our lowest-porosity samples (φ_0 = 12.7 and 14.2%), we use equation (1), inserting $\alpha = 1$ and $\nu = 0.15$ to calculate the differential stress that occurs upon reducing the pore pressure from 35 MPa to the current 8 MPa, that is, $\Delta P_p = -27$ MPa (NAM, 2016). The result shows an increase from 22 to 44 MPa. For this stress window, Δe_t ranges from 0.11 to 0.33% (Figure 3a), so that S_a = 8 to 23 GPa. These values of S_a are in the same range as described in previous work (NAM, 2016). To determine the elastic component of these values of Δe_t, we used our cumulative elastic axial strain data obtained for $\dot{\varepsilon}_t \sim 10^{-9}$ s^{-1} (Figure 7c). Hence, for the above stress window, Δe_{el}^{Σ} = 0.08 to 0.15%, and the elastic stiffness S_{el} ranges from 18 to 34 GPa. These values of S_{el} are significantly stiffer than the range described for S_a. Moreover, they show that for Slochteren sandstones with $\varphi_0 < 21.6\%$, deformed at $\dot{\varepsilon}_t \sim 10^{-9}$ s^{-1}, 30 to 55% of the total axial strain accumulated upon simulated pore pressure depletion is dissipated through inelastic deformation and is therefore unavailable for seismicity. The implication is that at least for these porosities, the assumption of a poroelastic reservoir response to pore pressure reduction leads to an overestimation of the stored energy available in the reservoir rock for driving seismicity by as much as 30–55%. These values are likely higher for sandstones with $\varphi_0 \geq 21.6\%$, since previous compression experiments performed on Slochteren sandstone under uniaxial strain conditions have shown an increasing relative contribution of inelastic strain, with increasing initial porosity (Hol, Mossop, et al., 2015; Hol et al., 2018; Schutjens et al., 1995). Moreover, our experiments yielded a larger contribution of inelastic deformation with decreasing strain rate (Figure 7). Therefore, for strain rates relevant for production of the Groningen gas field (~10^{-12} s^{-1}; NAM, 2015), the relative contribution of inelastic compaction may be larger still. To realistically resolve the magnitude of inelastic and elastic compaction of the Slochteren reservoir for these low strain rates, a full constitutive microphysical model for sandstone deformation is required that describes the relationship between stress and strain, including effects of strain and loading rate, initial porosity, progressively developing inelastic strain, and concomitant stress changes.

8. Conclusions

We performed conventional triaxial compression experiments on Slochteren sandstone samples from the currently producing, seismogenic Groningen gas field. Each experiment was performed under in situ conditions of temperature and chemistry (T = 100 °C; 4.4 M saline brine; see Table 2) and consisted of (1) an in situ conditioning phase, in which samples were equilibrated to the predepletion stress state of $\sigma_3^{eff} = P_c^{eff}$ = 8 MPa and $(\sigma_1 - \sigma_3)$ = 22 MPa, in order to remove any preexisting damage induced during core retrieval and storage, and (2) a multistep phase, in which we employed successive stages of active axial loading and stress relaxation at P_c^{eff} = 15 MPa and $(\sigma_1 - \sigma_3)$ up to 50 MPa, to investigate the relative contributions of elastic strain and time-independent (plastic) and time-dependent (creep) inelastic strains. These stress changes were chosen to simulate pore pressure reduction in the field, assuming a poroelastic response of the reservoir to depletion. A poroelastic stress path was chosen to test whether Slochteren sandstones (φ_0 = 12–25%) behaved elastically under these conditions, while any inelastic strain development would demonstrate that inelastic compaction should accordingly be expected in the field. In addition, a quantitative microstructural comparison of undeformed and deformed samples was carried out in order to gain insights into the microphysical mechanisms accommodating inelastic strain.

1. The present incremental axial loading plus stress relaxation experiments showed that for the chosen poroelastic stress changes, inelastic axial strain developed throughout triaxial compression, reaching final values of 0.1 to 0.8%, versus 0.3 to 0.6% of elastic axial strain in the multistep phase. A substantial part of this inelastic strain constituted time-dependent deformation ($(e_{cr})_{fin}$ = 0.1–0.7%; Table 1).
2. The shape of each differential stress versus cumulative elastic axial strain curve was near linear to slightly concave up, with elastic strains generally increasing with increasing initial porosity and increasing strain rate (Figures 7a and 7c).

3. The shape of individual stress versus cumulative inelastic axial strain curves was nonlinear and concave down, revealing a strain hardening trend at decreasing rates. For a given stress, the magnitude of inelastic strain generally increased with increasing initial porosity and decreasing strain rate (Figures 7b and 7d).
4. Microstructures of deformed samples revealed that the deformation mechanisms operating during the present experiments were a combination of intergranular (grain boundary) cracking, intergranular slip, and intragranular/transgranular cracking (Figure 6). Crack density data showed that the importance of intragranular/transgranular cracking increased with increasing porosity (Table 3).
5. During stress relaxation stages, the mechanisms accommodating creep strain were inferred to be a combination of rate-dependent intergranular slip and stress-corrosion cracking leading to time-dependent grain failure (Figure 8). The importance of stress-corrosion cracking increased with increasing porosity.
6. The observations of continuous inelastic strain development, strain hardening, and a rate and porosity dependence of the magnitude of inelastic strain (Figures 7b and 7d) suggest that inelastic deformation in Slochteren sandstone is best described by a yield envelope, which expands with increasing inelastic strain, increasing strain rate, and decreasing initial porosity.
7. During the multistep phase, our samples with $\varphi_0 \geq 21.6\%$ revealed marked inelastic horizontal expansion (i.e., $e_i > -\Delta\varphi_i$; Figure 3b). This implies that at least in high-porosity regions within the reservoir, the assumption of poroelastic stress changes accompanying pore pressure depletion underestimated the change in the effective horizontal stress developing under assumed uniaxial strain conditions. In situ stress measurements appear to confirm this observation (van Eijs, 2015), confirming an inelastic contribution to in situ compaction.
8. Application of the data obtained on our samples with $\varphi_0 < 21.6\%$ at axial creep strain rates of ~10^{-9} s^{-1} showed that for the current state of pore pressure depletion ($\Delta P_p = -27$ MPa), 30 to 55% of the total strain energy was dissipated by inelastic deformation, and is therefore unavailable for seismicity, and other energy-dissipating processes associated with fault rupture. This effect is expected to be larger for higher porosities and lower strain rates (i.e., $<10^{-9}$ s^{-1}).
9. For strain rates relevant for gas production in the Groningen field (~10^{-12} s^{-1}), estimations of inelastic versus elastic strain partitioning require a full microphysical model, incorporating effects of initial porosity, strain or loading rate, and progressively developing inelastic strain on yield envelope expansion and hence stress-strain behavior. Such a microphysical model is currently under development and may in future work be implemented in larger-scale seismological models.

Appendix A: List of Key Symbols

e_t	total axial strain ($\Delta L/L_0$)
$\dot{\varepsilon}_t$	total axial strain rate
$\dot{\varepsilon}_{cr}$	axial creep strain rate
$(\sigma_1 - \sigma_3)_{max}$	maximum differential stress imposed
$(e_t)_{fin}$	final total axial strain measured at the end of each phase
$(e_i)_{fin}$	final inelastic axial strain measured at the end of each phase
$(e_{el})_{fin}$	final elastic axial strain at the end of each phase: $(e_t)_{fin} - (e_i)_{fin}$
$(e_i^{inst})_{max}$	sum of all instantaneous axial strains of all active loading stages
$(e_{cr})_{max}$	sum of all axial creep strains of all relaxation stages
$(e_i^{\Sigma})_{max}$	maximum cumulative inelastic axial strain: $(e_i^{inst})_{max} + (e_{cr})_{max}$
$(e_{el}^{\Sigma})_{max}$	maximum cumulative elastic axial strain: $(e_t)_{max} - (e_i^{\Sigma})_{max}$
$\Delta\varphi_t$	total porosity change ($\Delta V_{pore}/V_0$)
$(\Delta\varphi_t)_{fin}$	final total porosity change measured at the end of each phase
$(\Delta\varphi_i)_{fin}$	final inelastic porosity change measured at the end of each phase
$(\Delta\varphi_{el})_{fin}$	final elastic porosity change at the end of each phase: $(\Delta\varphi_t)_{fin} - (\Delta\varphi_i)_{fin}$
E_a	apparent (quasi-elastic) Young's modulus: $\Delta(\sigma_1 - \sigma_3)/\Delta e_t$
S_a	apparent (elastic + inelastic) stiffness: $-\Delta P_p/\Delta e_t$
S_{el}	elastic stiffness: $-\Delta P_p/\Delta e_{el}^{\Sigma}$

Acknowledgments
This research was carried out in the context of the research program funded by the Nederlandse Aardolie Maatschappij (NAM). Initiated in late 2014, this program aims to fundamentally improve understanding of production-induced reservoir compaction and seismicity in the seismogenic Groningen gas field. We thank the NAM and Shell Global Solutions for providing samples and data and the NAM for allowance to publish this study. Specifically, the authors like to thank the involved teams at Shell Global Solutions and NAM for numerous useful scientific interactions. Colin Peach is thanked for advice and help both in and outside of the lab. We thank UU employees Gert Kastelein, Thony van der Gon-Netscher, Floris van Oort, Peter van Krieken, and Eimert de Graaff for technical assistance. Finally, we would like to thank Dirk Doornhof and two anonymous reviewers for their constructive comments that helped increase the quality of this paper. The data for this paper are available as Pijnenburg, Ronald; Verberne, Berend; Hangx, Suzanne; and Spiers, Christopher (2018): Mechanical and microstructural data used in the article Pijnenburg et al., Deformation behavior of sandstones from the seismogenic Groningen gas field: Role of inelastic versus elastic mechanisms. GFZ Data Services: http://doi.org/10.5880/fidgeo.2018.005.

References

Altmann, J. B., Müller, T. M., Müller, B. I. R., Tingay, M. R. P., & Heidbach, O. (2010). Poroelastic contribution to the reservoir stress path. *International Journal of Rock Mechanics and Mining Sciences*, *47*(7), 1104–1113. https://doi.org/10.1016/j.ijrmms.2010.08.001

Amthor, J. E., & Okkerman, J. (1998). Influence of early diagenesis on reservoir quality of Rotliegend sandstones, northern Netherlands. *American Association of Petroleum Geologists Bulletin*, *82*, 2246–2265.

Ashby, M. F., & Sammis, C. G. (1990). The damage mechanics of brittle solids in compression. *Pure and Applied Geophysics*, *133*(3), 489–521. https://doi.org/10.1007/BF00878002

Bardainne, T., Dubos-sallée, N., Sénéchal, G., Gaillot, P., & Perroud, H. (2008). Analysis of the induced seismicity of the Lacq gas field (southwestern France) and model of deformation. *Geophysical Journal International*, *172*(3), 1151–1162. https://doi.org/10.1111/j.1365-246X.2007.03705.x

Baud, P., Klein, E., & Wong, T. (2004). Compaction localization in porous sandstones: Spatial evolution of damage and acoustic emission activity. *Journal of Structural Geology*, *26*(4), 603–624. https://doi.org/10.1016/j.jsg.2003.09.002

Baud, P., Vajdova, V., & Wong, T. F. (2006). Shear-enhanced compaction and strain localization: Inelastic deformation and constitutive modeling of four porous sandstones. *Journal of Geophysical Research*, *111*, B12401. https://doi.org/10.1029/2005JB004101

Baud, P., Wong, T. F., & Zhu, W. (2014). Effects of porosity and crack density on the compressive strength of rocks. *International Journal of Rock Mechanics and Mining Sciences*, *67*, 202–211. https://doi.org/10.1016/j.ijrmms.2013.08.031

Baud, P., Zhu, W., & Wong, T. (2000). Failure mode and weakening effect of water on sandstone. *Journal of Geophysical Research*, *105*, 371–389. https://doi.org/10.1029/2000JB900087

Bernabe, Y., Fryer, D. T., & Hayes, J. A. (1992). The effect of cement on the strength of granular rocks. *Geophysical Research Letters*, *19*, 1511–1514. https://doi.org/10.1029/92GL01288

Bernabe, Y., Fryer, D. T., & Shively, R. M. (1994). Experimental-observations of the elastic and inelastic behavior of porous sandstones. *Geophysical Journal International*, *117*(2), 403–418. https://doi.org/10.1111/j.1365-246X.1994.tb03940.x

Borg, I. Y., Friedman, M., Handin, J., & Higgs, D. V. (1960). Experimental deformation of St. Peter sand: A study of cataclastic flow. *Memoirs-Geological Society of America*, *79*, 133–192. https://doi.org/10.1130/MEM79-p133

Bouckovalas, G. D., Andrianopoulos, K. I., & Papadimitriou, A. G. (2003). A critical state interpretation for the cyclic liquefaction resistance of silty sands. *Soil Dynamics and Earthquake Engineering*, *23*(2), 115–125. https://doi.org/10.1016/S0267-7261(02)00156-2

Bourne, S. J., Oates, S. J., Bommer, J. J., Dost, B., Van Elk, J., & Doornhof, D. (2015). A Monte Carlo method for probabilistic hazard assessment of induced seismicity due to conventional natural gas production. *Bulletin of the Seismological Society of America*, *105*(3), 1721–1738. https://doi.org/10.1785/0120140302

Bourne, S. J., Oates, S. J., Van Elk, J., & Doornhof, D. (2014). A seismological model for earthquakes induced by fluid extraction from a subsurface reservoir. *Journal of Geophysical Research: Solid Earth*, *119*, 8991–9015. https://doi.org/10.1002/2014JB011663

Brantut, N., Heap, M. J., Baud, P., & Meredith, P. G. (2014). Rate- and strain-dependent brittle deformation of rocks. *Journal of Geophysical Research: Solid Earth*, *119*, 1818–1836. https://doi.org/10.1002/2013JB010448

Brantut, N., Heap, M. J., Meredith, P. G., & Baud, P. (2013). Time-dependent cracking and brittle creep in crustal rocks: A review. *Journal of Structural Geology*, *52*, 17–43. https://doi.org/10.1016/j.jsg.2013.03.007

Breckels, I. M., & van Eekelen, H. A. M. (1982). Relationship between horizontal stress and depth in sedimentary basins. *Journal of Petroleum Technology*, *34*(09), 2191–2199. https://doi.org/10.2118/10336-PA

Brouwer, A. S., van den Broek, M., Zappa, W., Turkenburg, W. C., & Faaij, A. (2016). Least-cost options for integrating intermittent renewables in low-carbon power systems. *Applied Energy*, *161*, 48–74. https://doi.org/10.1016/j.apenergy.2015.09.090

Brzesowsky, R. H., Hangx, S. J. T., Brantut, N., & Spiers, C. J. (2014). Compaction creep of sands due to time-dependent grain failure: Effects of chemical environment, applied stress and grain size. *Journal of Geophysical Research: Solid Earth*, *119*, 7521–7541. https://doi.org/10.1002/2014JB011277

Brzesowsky, R. H., Spiers, C. J., Peach, C. J., & Hangx, S. J. T. (2011). Failure behavior of single sand grains: Theory versus experiment. *Journal of Geophysical Research*, *116*, B06205. https://doi.org/10.1029/2010JB008120

Brzesowsky, R. H., Spiers, C. J., Peach, C. J., & Hangx, S. J. T. (2014). Time-independent compaction behavior of quartz sands. *Journal of Geophysical Research: Solid Earth*, *119*, 5814–5829. https://doi.org/10.1002/2014JB011151

Buijze, L., van den Bogert, P. A. J., Wassing, B. B. T., Orlic, B., & Ten Veen, J. (2017). Fault reactivation mechanisms and dynamic rupture modelling of depletion-induced seismic events in a Rotliegend gas reservoir. *Netherlands Journal of Geosciences*, *96*(5), s131–s148. https://doi.org/10.1017/njg.2017.27

Chang, C., Zoback, M. D., & Khaksar, A. (2006). Empirical relations between rock strength and physical properties in sedimentary rocks. *Journal of Petroleum Science and Engineering*, *51*(3-4), 223–237. https://doi.org/10.1016/j.petrol.2006.01.003

Chester, J. S., Lenz, S. C., Chester, F. M., & Lang, R. A. (2004). Mechanisms of compaction of quartz sand at diagenetic conditions. *Earth and Planetary Science Letters*, *220*(3-4), 435–451. https://doi.org/10.1016/S0012-821X(04)00054-8

Chuhan, F. A., Kjeldstad, A., Bjørlykke, K., & Høeg, K. (2002). Porosity loss in sand by grain crushing—Experimental evidence and relevance to reservoir quality. *Marine and Petroleum Geology*, *19*(1), 39–53. https://doi.org/10.1016/S0264-8172(01)00049-6

Cook, J. E., Goodwin, L. B., Boutt, D. F., & Tobin, H. J. (2015). The effect of systematic diagenetic changes on the mechanical behavior of a quartz-cemented sandstone. *Geophysics*, *80*(2), D145–D160. https://doi.org/10.1190/Geo2014-0026.1

Cooke, M. L., & Madden, E. H. (2014). Is the earth lazy? A review of work minimization in fault evolution. *Journal of Structural Geology*, *66*, 334–346. https://doi.org/10.1016/j.jsg.2014.05.004

Cuisiat, F., Jostad, H. P., Andresen, L., Skurtveit, E., Skomedal, E., Hettema, M., & Lyslo, K. (2010). Geomechanical integrity of sealing faults during depressurisation of the Statfjord Field. *Journal of Structural Geology*, *32*(11), 1754–1767. https://doi.org/10.1016/j.jsg.2010.01.006

Darling, T. W. (2004). Neutron diffraction study of the contribution of grain contacts to nonlinear stress-strain behavior. *Geophysical Research Letters*, *31*, L16604. https://doi.org/10.1029/2004GL020463

David, C., Menendez, B., Zhu, W., & Wong, T. F. (2001). Mechanical compaction, microstructures and permeability evolution in sandstones. *Physics and Chemistry of the Earth Part A Solid Earth and Geodesy*, *26*(1-2), 45–51. https://doi.org/10.1016/S1464-1895(01)00021-7

David, E. C., Brantut, N., Schubnel, A., & Zimmerman, R. W. (2012). Sliding crack model for nonlinearity and hysteresis in the uniaxial stress–strain curve of rock. *International Journal of Rock Mechanics and Mining Sciences*, *52*, 9–17. https://doi.org/10.1016/j.ijrmms.2012.02.001

Davies, R., Foulger, G., Bindley, A., & Styles, P. (2013). Induced seismicity and hydraulic fracturing for the recovery of hydrocarbons. *Marine and Petroleum Geology*, *45*, 171–185. https://doi.org/10.1016/j.marpetgeo.2013.03.016

De Freitas, M. H., & Dobereiner, L. (1986). Geotechnical properties of weak sandstones. *Géotechnique*, *36*(1), 79–94. https://doi.org/10.1680/geot.1986.36.1.79

De Jager, J., Doyle, M. A., Grantham, P. J., & Mabillard, J. E. (1996). Hydrocarbon habitat of the West Netherlands Basin. In H. E. Rondeel, D. A. J. Batjes, & W. H. Nieuwenhuijs (Eds.), *Geology of gas and oil under the Netherlands* (p. 1996). Dordrecht: Kluwer Academic Publishers. https://doi.org/10.1007/978-94-009-0121-6_17

De Waal, J. A. (1986). *On the rate type compaction behaviour of sandstone reservoir rock*. Delft, Netherlands: Delft University.

De Waal, J. A., Muntendam-Bos, A. G., & Roest, J. P. A. (2017). From checking deterministic predictions to probabilities, scenarios and control loops for regulatory supervision. *Netherlands Journal of Geosciences*, *96*(05), s17–s25. https://doi.org/10.1017/njg.2017.15

Dewers, T., & Hajash, A. (1995). Rate laws for water-assisted compaction and stress-induced water-rock interaction in sandstones. *Journal of Geophysical Research*, *100*, 13,093–13,112. https://doi.org/10.1029/95JB00912

Diaz, G., Kittl, P., & Rosales, M. (2003). Probabilistic design and quality control in probabilistic strength of materials. *International Journal of Solids and Structures*, *40*(19), 5001–5015. https://doi.org/10.1016/S0020-7683(03)00251-8

Dieterich, J. H. (1972). Time-dependent friction in rocks. *Journal of Geophysical Research*, *77*(20), 3690–3697. https://doi.org/10.1029/JB077i020p03690

Dieterich, J. H. (1978). Time-dependent friction and the mechanics of stick-slip. *Pure and Applied Geophysics*, *116*(4–5), 790–806. https://doi.org/10.1007/BF00876539

DiGiovanni, A. A., Fredrich, J. T., Holcomb, D. J., & Olsson, W. A. (2007). Microscale damage evolution in compacting sandstone. *Geological Society of London, Special Publication*, *289*(1), 89–103. https://doi.org/10.1144/SP289.6

Doser, D. I., Baker, M. R., & Mason, D. B. (1991). Seismicity in the War-Wink gas field, Delaware Basin, West Texas, and its relationship to petroleum production. *Bulletin of the Seismological Society of America*, *81*(3), 971–986. https://doi.org/10.1016/0148-9062(92)93679-E

Dzung, T. Q., Al-Harthy, M., Hunt, S., & Sayers, J. (2009). The impact of uncertainty on subsidence and compaction prediction. *Science, Technology and Development*, *12*(6), 84–95.

Eberhart-Phillips, D., & Oppenheimer, D. H. (1984). Induced seismicity in The Geysers Geothermal Area, California. *Journal of Geophysical Research*, *89*(B2), 1191–1207. https://doi.org/10.1029/JB089iB02p01191

Estrada, N., Lizcano, A., & Taboada, A. (2010a). Simulation of cemented granular materials: I. Macroscopic stress-strain response and strain localization. *Physical Review. E, Statistical, Nonlinear, and Soft Matter Physics*, *82*(1). https://doi.org/10.1103/PhysRevE.82.011303

Estrada, N., Lizcano, A., & Taboada, A. (2010b). Simulation of cemented granular materials: II. Micromechanical description and strength mobilization at the onset of macroscopic yielding. *Physical Review. E, Statistical, Nonlinear, and Soft Matter Physics*, *82*(1). https://doi.org/10.1103/PhysRevE.82.011304

Fialko, Y., & Simons, M. (2000). Deformation and seismicity in the Coso geothermal area, Inyo County, California: Observations and modeling using satellite radar interferometry. *Journal of Geophysical Research*, *105*, 21,781–21,793. https://doi.org/10.1029/2000JB900169

GEA (2012). In T. B. Johansson, et al. (Eds.), *Summaries*. Laxenburg, Austria: Cambridge University Press.

Geertsma, J. (1973). Land subsidence above compacting oil and gas reservoirs. *Journal of Petroleum Technology*, *25*(06), 734–744. https://doi.org/10.2118/3730-PA

Glennie, K. W. (1972). Permian Rotliegendes of Northwest Europe interpreted in the light of modern desert sedimentation studies. *American Association of Petroleum Geologists Bulletin*, *56*, 1048–1071.

Grasso, J. R. (1992). Mechanics of seismic instabilities induced by the recovery of hydrocarbons. *Pure and Applied Geophysics*, *139*(3–4), 507–534. https://doi.org/10.1007/BF00879949

Gratier, J. P., & Guiguet, R. (1986). Experimental pressure solution-deposition on quartz grains: The crucial effect of the nature of the fluid. *Journal of Structural Geology*, *8*(8), 845–856. https://doi.org/10.1016/0191-8141(86)90030-1

Grotsch, J., Sluijk, A., van Ojik, K., De Keijzerm, M., Graaf, J., & Steenbrink, J. (2011). The Groningen gas field: Fifty years of exploration and gas production from a permian dryland reservoir. In *The Permian Rotliegend of the Netherlands* (Vol. 98, pp. 11–33). Tulsa, OK: Society for Sedimentary Geology.

Guéguen, Y., & Fortin, J. (2013). Elastic envelopes of porous sandstones. *Geophysical Research Letters*, *40*, 3550–3555. https://doi.org/10.1002/grl.50676

Guyer, R. A. (2006). Hysteretic elastic systems: Geophysical materials. *Sci. Hysteresis*, *3*, 555–688. https://doi.org/10.1016/B978-012480874-4/50024-5

Hangx, S. J. T., Spiers, C. J., & Peach, C. J. (2010a). Creep of simulated reservoir sands and coupled chemical-mechanical effects of CO_2 injection. *Journal of Geophysical Research*, *115*, B09205. https://doi.org/10.1029/2009JB006939

Hangx, S. J. T., Spiers, C. J., & Peach, C. J. (2010b). Mechanical behavior of anhydrite caprock and implications for CO_2 sealing capacity. *Journal of Geophysical Research*, *115*, B07402. https://doi.org/10.1029/2009JB006954

Heap, M. J., P. Baud, P. G. Meredith, A. F. Bell, & I. G. Main (2009). Time-dependent brittle creep in Darley Dale sandstone. *Journal of Geophysical Research*, *114*, B07203. https://doi.org/10.1029/2008JB006212

Heap, M. J., Brantut, N., Baud, P., & Meredith, P. G. (2015). Time-dependent compaction band formation in sandstone. *Journal of Geophysical Research: Solid Earth*, *120*, 4808–4830. https://doi.org/10.1002/2015JB012022

Hettema, M., Papamichos, E., & Schutjens, P. (2002). Subsidence delay: Field observations and analysis. *Oil & Gas Science and Technology*, *57*(5), 443–458. https://doi.org/10.2516/ogst:2002029

Hettema, M., Schutjens, P. M., Verboom, B., & Gussinklo, H. (2000). Production-induced compaction of a sandstone reservoir: The strong influence of stress path. *SPE Reservoir Evaluation and Engineering*, *3*(04), 342–347. https://doi.org/10.2118/65410-PA

Hol, S., Mossop, A. P., van der Linden, A. J., Zuiderwijk, P. M. M., & Makurat, A. H. (2015). *Long-term compaction behavior of Permian sandstones—An investigation into the mechanisms of subsidence in the Dutch Wadden Sea* (pp. 15–618). Alexandria, VA: ARMA.

Hol, S., van der Linden, A., Bierman, S., Marcelis, F., & Makurat, A. (2018). Rock physical controls on production-induced compaction in the Groningen Field. *Scientific Reports*, *8*, 7156.

Hol, S., A. J. van der Linden, P. M. M. Zuiderwijk, F. H. M. Marcelis, & A. H. Coorn (2015). Mechanical characterization of Permian reservoir sandstone from the Moddergat-3 well in the Dutch Wadden Area (Report, Shell Global Solutions International B.V., Rijswijk).

Holt, R. M., Brignoli, M., & Kenter, C. J. (2000). Core quality: Quantification of coring-induced rock alteration. *International Journal of Rock Mechanics and Mining Sciences*, *37*(6), 889–907. https://doi.org/10.1016/S1365-1609(00)00009-5

Hunfeld, L. B., Niemeijer, A. R., & Spiers, C. J. (2017). Frictional properties of simulated fault gouges from the seismogenic Groningen Gas Field under in situ P-T chemical conditions. *Journal of Geophysical Research: Solid Earth*, *122*, 8969–8989. https://doi.org/10.1002/2017JB014876

IEA (2016). Key world energy trends. In *World energy balances* (pp. 3–19). Paris: International Energy Agency, OECD Publishing.

Jaeger, J. C., Cook, N. G. W., & Zimmerman, R. W. (2007). *Fundamentals of rock mechanics* (4th ed.). Malden: Blackwell Publishing.

Karner, S. L., Chester, F. M., & Chester, J. S. (2005). Towards a general state-variable constitutive relation to describe granular deformation. *Earth and Planetary Science Letters*, *237*(3–4), 940–950. https://doi.org/10.1016/j.epsl.2005.06.056

Karner, S. L., Chester, F. M., Kronenberg, A. K., & Chester, J. S. (2003). Subcritical compaction and yielding of granular quartz sand. *Tectonophysics*, *377*(3–4), 357–381. https://doi.org/10.1016/j.tecto.2003.10.006

Karner, S. L., Chester, J. S., Chester, F. M., Kronenberg, A. K., & Hajash, A. (2005). Laboratory deformation of granular quartz sand: Implications for the burial of clastic rocks. *American Association of Petroleum Geologists Bulletin*, *89*(5), 603–625. https://doi.org/10.1306/12200404010

Kemeny, J. M., & Cook, N. G. W. (1991). Micromechanics of deformation in rocks. In S. P. Shah (Ed.), *Toughening mechanisms in quasi-brittle materials* (pp. 155–188). Dordrecht, Netherlands: Springer. https://doi.org/10.1007/978-94-011-3388-3_10

Ketelaar, V. B. H. (2009). In F. D. van der Meer (Ed.), *Satellite radar interferometry: Subsidence monitoring techniques*. New York: Springer. https://doi.org/10.1007/978-1-4020-9428-6

Klein, E., Baud, P., Reuschle, T., & Wong, T. (2001). Mechanical behaviour and failure mode of Bentheim sandstone under triaxial compression. *Physics and Chemistry of the Earth*, *26*(1–2), 21–25. https://doi.org/10.1016/S1464-1895(01)00017-5

Koster, H. R. A., & van Ommeren, J. (2015). A shaky business: Natural gas extraction, earthquakes and house prices. *European Economic Review*, *80*, 120–139. https://doi.org/10.1016/j.euroecorev.2015.08.011

Lawn, B. (1993). In E. A. Davis & I. M. Ward (Eds.), *Fracture of brittle solids* (2nd ed.). Cambridge: Cambridge University Press.

Lele, S., Hsu, Y.-S., Garzon, J. L., DeDontney, N., Searles, K. H., Gist, G. A., et al. (2016). Geomechanical modeling to evaluate production-induced seismicity at the Groningen field, SPE Int., (183554).

Lu, C., Danzer, R., & Fischer, F. D. (2002). Fracture statistics of brittle materials: Weibull or normal distribution. *Physical Review. E, Statistical, Nonlinear, and Soft Matter Physics*, *65*(6). https://doi.org/10.1103/PhysRevE.65.067102

Mallman, E. P., & Zoback, M. D. (2007). Subsidence in the Louisiana coastal zone due to hydrocarbon production. *Journal of Coastal Research*, *233*, 771–786. https://doi.org/10.2112/05-0553

Marone, C. (1998). Laboratory-derived friction laws and their application to seismic faulting. *Annual Review of Earth and Planetary Sciences*, *26*(1), 643–696. https://doi.org/10.1146/annurev.earth.26.1.643

McBride, E. (1963). A classification of common sandstones. *Journal of Sedimentary Research*, *33*(3), 664–669. https://doi.org/10.1306/74D70EE8-2B21-11D7-8648000102C1865D

McBride, E. F. (1989). Quartz cement in sandstones: A review. *Earth-Science Reviews*, *26*(1-3), 69–112. https://doi.org/10.1016/0012-8252(89)90019-6

Mcgarr, A. (1999). On relating apparent stress to the stress causing earthquake fault slip. *Journal of Geophysical Research*, *104*, 3003–3011. https://doi.org/10.1029/1998JB900083

Menéndez, B., Zhu, W., & Wong, T.-F. (1996). Micromechanics of brittle faulting and cataclastic flow in Berea sandstone. *Journal of Structural Geology*, *18*(1), 1–16. https://doi.org/10.1016/0191-8141(95)00076-P

Mitchell, J. K., & Green, R. A. (2017). Some induced seismicity considerations in geo-energy resource development. *Geomechanics for Energy and the Environment*, *10*, 3–11. https://doi.org/10.1016/j.gete.2017.01.001

Morton, R. A., Purcell, N. A., & Peterson, R. (2001). Field evidence of subsidence and faulting induced by hydrocarbon production in coastal southeast Texas. *Gulf Coast Association of Geological Societies Transactons*, *L1*, 239–248.

Mossop, A., & Segall, P. (1997). Subsidence at The Geysers Geothermal Field, N. California from a comparison of GPS and leveling surveys. *Geophysical Research Letters*, *24*, 1839–1842. https://doi.org/10.1029/97GL51792

Mulders, F. M. M. (2003). *Modelling of stress development and fault slip in and around a producing gas reservoir*. Delft, Netherlands: Delft University.

NAM (2013). Technical Addendum to the Winningsplan Groningen 2013 Subsidence, Induced Earthquakes and Seismic Hazard Analysis in the Groningen Field.

NAM (2015). Bodemdaling door Aardgaswinning. NAM-gasvelden in Groningen, Friesland, en het noorden van Drenthe.

NAM (2016). Technical Addendum to the Winningsplan Groningen 2016.

Niemeijer, A. R., & Spiers, C. J. (2007). A microphysical model for strong velocity weakening in phyllosilicate-bearing fault gouges. *Journal of Geophysical Research*, *112*, B10405. https://doi.org/10.1029/2007JB005008

Niemeijer, A. R., Spiers, C. J., & Bos, B. (2002). Compaction creep of quartz sand at 400 ^ 600^{3}C: Experimental evidence for dissolution-controlled pressure solution. *Earth and Planetary Science Letters*, *195*(3-4), 261–275. https://doi.org/10.1016/S0012-821X(01)00593-3

Ord, A., Vardoulakis, I., & Kajewski, R. (1991). Shear band formation in Gosford sandstone. *International Journal of Rock Mechanics and Mining Sciences*, *28*(5), 397–409. https://doi.org/10.1016/0148-9062(91)90078-Z

Paterson, M. S., & Wong, T. F. (2005). *Experimental rock deformation—The brittle field*. New York: Springer.

Peach, C. J. (1991). *Influence of deformation on the fluid transport properties of salt rocks*. Utrecht, Netherlands: Geologica Ultraiectina, Utrecht University.

Pratt, W. E., & Johnson, D. W. (1926). Local subsidence of the Goose creek oil field. *Journal of Geology*, *170*(4), 520–529. https://doi.org/10.1086/521238

Preibisch, S., Saalfeld, S., & Tomancak, P. (2009). Globally optimal stitching of tiled 3D microscopic image acquisitions. *Bioinformatics*, *25*(11), 1463–1465. https://doi.org/10.1093/bioinformatics/btp184

Renard, F., Park, A., Ortoleva, P., & Gratier, J. P. (1999). An integrated model for transitional pressure solution in sandstones. *Tectonophysics*, *312*(2–4), 97–115. https://doi.org/10.1016/S0040-1951(99)00202-4

Rijken, M. C. M. (2005). *Modeling naturally fractured reservoirs: From experimental rock mechanics to flow simulation*. Austin: The University of Texas.

Rutter, E. H. (1983). Pressure solution in nature, theory and experiment. *Journal of the Geological Society of London*, *140*(5), 725–740. https://doi.org/10.1144/gsjgs.140.5.0725

Rutter, E. H., & Glover, C. T. (2012). The deformation of porous sandstones: Are Byerlee friction and the critical state line equivalent? *Journal of Structural Geology*, *44*, 129–140.

Rutter, E. H., & Mainprice, D. H. (1978). The effect of water on stress relaxation of faulted and unfaulted sandstone. *Pure and Applied Geophysics*, *116*(4–5), 634–654. https://doi.org/10.1007/BF00876530

Sackfield, A., & Hills, D. A. (1986). The strength of some non-hertzian plane contacts. *Journal of Tribology*, *108*(4), 655. https://doi.org/10.1115/1.3261296

Saidi, F., Bernabe, Y., & Reuschle, T. (2003). The mechanical behaviour of synthetic, poorly consolidated granular rock under uniaxial compression. *Tectonophysics*, *370*(1–4), 105–120. https://doi.org/10.1016/S0040-1951(03)00180-X

Sakic, A., Nanver, L. K., van Veen, G., Kooijman, K., Vogelsang, P., Scholtes, T. L. M., et al. (2011). Solid-state backscattered-electron detector for sub-keV imaging in Scanning Electron Microscopy. In *ICT Open: Micro technology and micro devices SAFE* (pp. 1–4). Veldhoven: Technology Foundation STW.

Santarelli, F., Tronvoll, J., Svennekjaer, M., Skeie, H., Henriksen, R., & Bratli, R. K. (1998). Reservoir stress path: The depletion and the rebound, SPE/ISRM Rock … , 1–7.

Santarelli, F. J., & Dusseault, M. B. (1991). Core quality control in petroleum engineering. In J. C. Roegiers (Ed.), *Rock mechanics as a multi-disciplinary science* (pp. 111–120). Rotterdam: Balkema.

Scholz, C. H. (2002). "The mechanics of earthquakes and faulting—Second edition" by Christopher H. Scholz. *Seismological Research Letters*, *74*, 333–333. https://doi.org/10.1785/gssrl.74.3.333

Schutjens, P. M. T. M. (1991). Experimental compaction of quartz sand at low effective stress and temperature conditions. *Journal of the Geological Society of London*, *148*(3), 527–539. https://doi.org/10.1144/gsjgs.148.3.0527

Schutjens, P. M. T. M., Fens, T. W., & Smits, R. M. M. (1995). Experimental observations of the uniaxial compaction of quartz-rich reservoir rock at stresses up to 80 MPa. In F. B. J. Barends, F. J. J. Brouwer, & F. H. Schroder (Eds.), *Land Subsidence* (pp. 389–409). Rotterdam, Netherlands: Balkema Publications.

Segall, P., & Fitzgerald, S. D. (1998). A note on induced stress changes in hydrocarbon and geothermal reservoirs. *Tectonophysics*, *289*(1-3), 117–128. https://doi.org/10.1016/S0040-1951(97)00311-9

Shalev, E., Lyakhovsky, V., Ougier-Simonin, A., Hamiel, Y., & Zhu, W. (2014). Inelastic compaction, dilation and hysteresis of sandstones under hydrostatic conditions. *Geophysical Journal International*, *197*(2), 920–925. https://doi.org/10.1093/gji/ggu052

Sharp, J. M., & Hill, D. W. (1995). Land subsidence along the northeastern Texas Gulf coast: Effects of deep hydrocarbon production. *Environmental Geology*, *25*(3), 181–191. https://doi.org/10.1007/BF00768547

Shen, Z., Jiang, M., & Thornton, C. (2016). DEM simulation of bonded granular material: Part I: Contact model and application to cemented sand. *Computers and Geotechnics*, *75*, 192–209. https://doi.org/10.1016/j.compgeo.2016.02.007

Shipton, Z. K., Evans, J. P., Abercrombie, R. E., & Brodsky, E. E. (2013). The missing sinks: Slip localization in faults , damage zones, and the seismic energy budget. In R. Abercrombie, A. McGarr, G. Di Toro, & K. Hiroo (Eds.), *Earthquakes: Radiated energy and the physics of faulting* (pp. 217–222). Washington, DC: American Geophysical Union.

Skurtveit, E., Torabi, A., Gabrielsen, R. H., & Zoback, M. D. (2013). Experimental investigation of deformation mechanisms during shear-enhanced compaction in poorly lithified sandstone and sand. *Journal of Geophysical Research: Solid Earth*, *118*, 4083–4100. https://doi.org/10.1002/jgrb.50342

Spiers, C. J., De Meer, S., Niemeijer, A. R., & Zhang, X. (2004). Kinetics of rock deformation by pressure solution and the role of thin aqueous films.

Spiers, C. J., Hangx, S. J. T., & Niemeijer, A. R. (2017). New approaches in experimental research on rock and fault behaviour in the Groningen gas field. *Netherlands Journal of Geosciences*, *96*(05), s55–s69. https://doi.org/10.1017/njg.2017.32

Suckale, J. (2009). *Induced seismicity in hydrocarbon fields*. Amsterdam: Elsevier. https://doi.org/10.1016/S0065-2687(09)05107-3

Tada, R., & Siever, R. (1989). Pressure solution during diagenesis. *Annual Review of Earth and Planetary Sciences*, *264*(5586), 511–512. https://doi.org/10.1038/264511b0

Tembe, S., Baud, P., & Wong, T. F. (2008). Stress conditions for the propagation of discrete compaction bands in porous sandstone. *Journal of Geophysical Research*, *113*, B09409. https://doi.org/10.1029/2007JB005439

Tembe, S., Vajdova, V., Baud, P., Zhu, W., & fong Wong, T. (2007). A new methodology to delineate the compactive yield cap of two porous sandstones under undrained condition. *Mechanics of Materials*, *39*(5), 513–523. https://doi.org/10.1016/j.mechmat.2006.08.005

Tengattini, A., Das, A., Nguyen, G. D., Viggiani, G., Hall, S. A., & Einav, I. (2014). A thermomechanical constitutive model for cemented granular materials with quantifiable internal variables: Part I—Theory. *Journal of the Mechanics and Physics of Solids*, *70*, 281–296. https://doi.org/10.1016/j.jmps.2014.05.021

Underwood, E. E. (1970). *Quantitative stereology*. Reading, MA: Addison Wesley.

van den Bogert, P. A. J. (2015). *Impact of various modelling options on the onset of fault slip and fault slip response using 2-dimensional finite-element modelling*. Assen: NAM.

van der Voort, N., & Vanclay, F. (2015). Social impacts of earthquakes caused by gas extraction in the province of Groningen, the Netherlands. *Environmental Impact Assessment Review*, *50*, 1–15. https://doi.org/10.1016/j.eiar.2014.08.008

Van Eijs, R. (2015). Neotectonic stresses in the Permian Slochteren Formation of the Groningen Field EP201510210531.

Van Eijs, R. M. H. E., Mulders, F. M. M., Nepveu, M., Kenter, C. J., & Scheffers, B. C. (2006). Correlation between hydrocarbon reservoir properties and induced seismicity in the Netherlands. *Engineering Geology*, *84*(3–4), 99–111. https://doi.org/10.1016/j.enggeo.2006.01.002

Van Noort, R., Visser, H. J. M., & Spiers, C. J. (2008). Influence of grain boundary structure on dissolution controlled pressure solution and retarding effects of grain boundary healing. *Journal of Geophysical Research*, *113*, B03201. https://doi.org/10.1029/2007JB005223

Van Thienen-Visser, K., Pruiksma, J. P., & Breunese, J. N. (2015). Compaction and subsidence of the Groningen gas field in the Netherlands. *Proceedings ofInternational Association of Hydrological Sciences*, *372*(10), 367–373. https://doi.org/10.5194/piahs-372-367-2015

Van Wees, J. D., Buijze, L., Van Thienen-Visser, K., Nepveu, M., Wassing, B. B. T., Orlic, B., & Fokker, P. A. (2014). Geomechanics response and induced seismicity during gas field depletion in the Netherlands. *Geothermics*, *52*, 206–219. https://doi.org/10.1016/j.geothermics.2014.05.004

Verberne, B. A., Spiers, C. J., Niemeijer, A. R., De Bresser, J. H. P., De Winter, D. A. M., & Plümper, O. (2013). Frictional properties and microstructure of calcite-rich fault gouges sheared at sub-seismic sliding velocities. *Pure and Applied Geophysics*, *171*(10), 2617–2640. https://doi.org/10.1007/s00024-013-0760-0

Waldmann, S. (2011). *Geological and mineralogical investigation of Rotliegend gas reservoirs in the Netherlands and their potential for CO_2 storage*. Jena, Germany: Jena University.

Waldmann, S., Busch, A., Van Ojik, K., & Gaupp, R. (2014). Importance of mineral surface areas in Rotliegend sandstones for modeling CO_2-water-rock interactions. *Chemical Geology*, *378–379*(1), 89–109. https://doi.org/10.1016/j.chemgeo.2014.03.014

Waldmann, S., & Gaupp, R. (2016). Grain-rimming kaolinite in Permian Rotliegend reservoir rocks. *Sedimentary Geology*, *335*, 17–33. https://doi.org/10.1016/j.sedgeo.2016.01.016

Walsh, J. B. (1965). The effect of cracks on the compressibility of rock. *Journal of Geophysical Research*, *70*, 381–389. https://doi.org/10.1029/JZ070i002p00381

Wang, H. F. (2000). *Theory of linear poroelasticity with applications to geomechanics and hydrogeology*. Mercer County, NJ: Princeton University Press.

Wassing, B. B. T., L. Buijze, & B. Orlic (2016). modelling of fault reactivation and fault slip in producing gas fields using a slip-weakening friction law, 50th US Rock Mech. /Geomech. Symp.

Weibull, W. (1951). A statistical distribution function of wide applicability. *Journal of Applied Mechanics*, *18*, 293–297.

Wong, T., & Wu, L. (1995). Tensile stress concentration and compressive failure in cemented granular material. *Geophysical Research Letters*, *22*, 1649–1652. https://doi.org/10.1029/95GL01596

Wong, T. F., & Baud, P. (1999). Mechanical compaction of porous sandstone. *Oil & Gas Science and Technology*, *54*(6), 715–727. https://doi.org/10.2516/ogst:1999061

Wong, T. F., & Baud, P. (2012). The brittle-ductile transition in porous rock: A review. *Journal of Structural Geology*, *44*, 25–53. https://doi.org/10.1016/j.jsg.2012.07.010

Wong, T. F., Christian, D., & Wenlu, Z. (1997). The transition from brittle faulting to cataclastic flow in porous sandstones: Mechanical deformation. *Journal of Geophysical Research*, *102*, 3009–3025. https://doi.org/10.1029/96JB03281

Wong, T.-F., Szeto, H., & Zhang, J. (1992). Effect of loading path and porosity on the failure mode of porous rocks. *Applied Mechanics Reviews*, *45*(8), 281–293. https://doi.org/10.1115/1.3119759

Xenaki, V. C., & Athanasopoulos, G. A. (2003). Liquefaction resistance of sand-silt mixtures: An experimental investigation of the effect of fines. *Soil Dynamics and Earthquake Engineering*, *23*(3), 183–194. https://doi.org/10.1016/S0267-7261(02)00210-5

Yale, D. P., & Swami, V. (2017). Conversion of dynamic mechanical property calculations to static values for geomechanical modeling, Am. Rock Mech. Assoc., 17–0644.

Yang, X.-S. (2000). Pressure solution in sedimentary basins: Effect of temperature gradient. *Earth and Planetary Science Letters*, *176*(2), 233–243. https://doi.org/10.1016/S0012-821X(99)00321-0

Yin, H., & Dvorkin, J. (1994). Strength of cemented grains. *Geophysical Research Letters*, *21*, 903–906. https://doi.org/10.1029/93GL03535

Zhang, J., Wong, T., & Davis, D. M. (1990). Micromechanics of pressure-induced grain Crushing in porous rocks. *95*, 341–352.

Ziegler, P. A. (1990). In Segunda Igreja Presbiteriana de Boa Vista (Ed.), *Geological atlas of western and central Europe* (2nd ed.). Bath: Geological Society Publishing House.

Zoback, M. D. (2007). Reservoir geomechanics, 12th Paper. Cambridge University Press. https://doi.org/10.1017/CBO9780511586477.